Draft version November 10, 2020
Typeset using LaTeX **preprint** style in AASTeX62

Initial Visible and Mid-IR Characterization of P/2019 LD_2 (ATLAS), an Active Transitioning Centaur Among the Trojans, with *Hubble*, *Spitzer*, ZTF, Keck, APO and GROWTH Imaging and Spectroscopy

Bryce T. Bolin,[1,2] Yanga R. Fernandez,[3] Carey M. Lisse,[4] Timothy R. Holt,[5,6] Zhong-Yi Lin,[7] Josiah N. Purdum,[8] Kunal P. Deshmukh,[9] James M. Bauer,[10] Eric C. Bellm,[11] Dennis Bodewits,[12] Kevin B. Burdge,[13] Sean J. Carey,[2] Chris M. Copperwheat,[14] George Helou,[2] Anna Y. Q. Ho,[1] Jonathan Horner,[5] Jan van Roestel,[13] Varun Bhalerao,[15] Chan-Kao Chang,[7] Christine Chen,[16,17] Chen-Yen Hsu,[7] Wing-Huen Ip,[7] Mansi M. Kasliwal,[13] Frank J. Masci,[2] Chow-Choong Ngeow,[7] Robert Quimby,[8,18] Rick Burruss,[19] Michael Coughlin,[20] Richard Dekany,[19] Alexandre Delacroix,[19] Andrew Drake,[1] Dmitry A. Duev,[1] Matthew Graham,[13] David Hale,[19] Thomas Kupfer,[21] Russ R. Laher,[2] Ashish Mahabal,[13,22] Przemyslaw J. Mróz,[13] James D. Neill,[13] Reed Riddle,[23] Hector Rodriguez,[24] Roger M. Smith,[23] Maayane T. Soumagnac,[25,26] Richard Walters,[13] Lin Yan,[27] and Jeffry Zolkower[19]

[1] *Division of Physics, Mathematics and Astronomy, California Institute of Technology, Pasadena, CA 91125, USA*
[2] *IPAC, Mail Code 100-22, Caltech, 1200 E. California Blvd., Pasadena, CA 91125, USA*
[3] *Department of Physics, University of Central Florida, Orlando, FL 32816, USA*
[4] *Johns Hopkins University Applied Physics Laboratory, Laurel, MD 20723*
[5] *Centre for Astrophysics, University of Southern Queensland, West Street, Toowoomba, QLD 4350, Australia*
[6] *Southwest Research Institute, Department of Space Studies, Boulder, CO-80302, USA*
[7] *Graduate Institute of Astronomy, National Central University, 32001, Taiwan*
[8] *Department of Astronomy, San Diego State University, 5500 Campanile Dr, San Diego, CA 92182, U.S.A.*
[9] *Department of Metallurgical Engineering and Materials Science, Indian Institute of Technology Bombay, Powai, Mumbai-400076, India*
[10] *Department of Astronomy, University of Maryland, College Park, MD 20742-0001, USA*
[11] *DIRAC Institute, Department of Astronomy, University of Washington, 3910 15th Avenue NE, Seattle, WA 98195, USA*
[12] *Physics Department, Leach Science Center, Auburn University, Auburn, AL 36832, U.S.A.*
[13] *Division of Physics, Mathematics and Astronomy, California Institute of Technology, Pasadena, CA 91125, U.S.A.*
[14] *Astrophysics Research Institute Liverpool John Moores University, 146 Brownlow Hill, Liverpool L3 5RF, United Kingdom*
[15] *Department of Physics, Indian Institute of Technology Bombay, Powai, Mumbai-400076, India*
[16] *Space Telescope Science Institute (STScI), 3700 San Martin Drive, Baltimore, MD 21218, USA*
[17] *Department of Physics and Astronomy, The Johns Hopkins University, 3701 San Martin Drive, Baltimore, MD 21218, USA*
[18] *Kavli Institute for the Physics and Mathematics of the Universe (WPI), The University of Tokyo Institutes for Advanced Study, The University of Tokyo, Kashiwa, Chiba 277-8583, Japan*
[19] *Caltech Optical Observatories, California Institute of Technology, Pasadena, CA 91125, U.S.A.*
[20] *School of Physics and Astronomy, University of Minnesota, Minneapolis, Minnesota 55455, USA*

Corresponding author: Bryce Bolin
bbolin@caltech.edu

[21]*Kavli Institute for Theoretical Physics, University of California, Santa Barbara, CA 93106, U.S.A.*
[22]*Center for Data Driven Discovery, California Institute of Technology, Pasadena, CA 91125, U.S.A.*
[23]*Caltech Optical Observatories, California Institute of Technology, Pasadena, CA 91125*
[24]*Caltech Optical Observatories, California Institute of Technology, Pasadena, CA 91125, U.S.A*
[25]*Lawrence Berkeley National Laboratory, 1 Cyclotron Road, Berkeley, CA 94720, U.S.A.*
[26]*Department of Particle Physics and Astrophysics, Weizmann Institute of Science, Rehovot 76100, Israel*
[27]*The Caltech Optical Observatories, California Institute of Technology, Pasadena, CA 91125, USA*

(Received –; Revised –; Accepted –)

Submitted to ApJL

ABSTRACT

We present visible and mid-infrared imagery and photometry of Jovian co-orbital comet P/2019 LD_2 taken with HST/WFC3 on 2020 April 1, Spitzer/IRAC on 2020 January 25, ZTF between 2019 April 9 and 2019 Nov 8 and the GROWTH telescope network from 2020 May to July, as well as visible spectroscopy from Keck/LRIS on 2020 August 19. Our observations indicate that the nucleus of LD_2 has a radius between 0.2-1.8 km assuming a 0.08 albedo and a coma dominated by $\sim$100μ m-scale dust ejected at $\sim$1 m/s speeds with a $\sim$1" jet pointing in the SW direction. LD_2 experienced a total dust mass loss of $\sim$$10^8$ kg and dust mass loss rate of $\sim$6 kg/s with Afρ/cross-section varying between $\sim$85 cm/125 km^2 and $\sim$200 cm/310 km^2 between 2019 April 9 and 2019 Nov 8. If the Afρ/cross-section increase remained constant, it implies LD_2's activity began $\sim$2018 November when within 4.8 au of the Sun, suggesting the onset of H_2O sublimation. We measure CO/CO_2 gas production of $\lesssim 10^{27}/\sim 10^{26}$ mol/s from our 4.5 μm Spitzer observations, colors of g-r = 0.59±0.03, r-i = 0.18±0.05, i-z = 0.01±0.07 from GROWTH observations, H_2O gas production of $\lesssim$80 kg/s from Keck/LRIS spectroscopy. We improve the orbital solution of LD_2 with our observations determining that the long-term orbit of LD_2 is similar to Jupiter Family Comets having close encounters with Jupiter within $\sim$0.5 Hill radius in the last $\sim$3 y, within 0.8 Hill radius in $\sim$9 y and has a 95% chance of being ejected from the Solar System in < 10 Myr.

Keywords: minor planets, asteroids: individual (P/2019 LD_2), temporarily captured orbiters, minimoons

1. INTRODUCTION

The gas giant Jupiter is the dominant gravitational perturbing body affecting the dynamical transfer of Solar System comets from the outer Solar System's trans-Neptunian disk beyond the orbit of Neptune into the inner reaches of the Solar System (Dones et al. 2015). The vast majority of comets in transfer from the outer Solar system regions such as the Oort Cloud in the case of long period comets (Vokrouhlický et al. 2019) or the trans-Neptunian region in the case of short period comets (Nesvorný et al. 2017). Once the comets originating from the trans-Neptunian region randomly walk their way through the outer Solar System and become strongly influenced by close-encounters with Jupiter, a significant portion are transformed in their orbital configuration into later joining the

Jupiter Family comet family or the Centaur group of small bodies. The Centaur class is defined as having semi-major axes, a, and perihelion, q, between 5.2 au, the semi-major axis, a_J of Jupiter, and 30.0 au, the semi-major axis of Neptune, a_N, (Jewitt 2009). An additional quantity used to define the Centaurs is the Tisserand parameter with respect to Jupiter, T_J, defined as

$$T_J = \frac{a_J}{a} + 2\sqrt{(1-e^2)\frac{a}{a_J}}\cos i \tag{1}$$

where e is the eccentricity of the body and i is the inclination as a rough indication of how much an object is influenced by the gravitational perturbations of Jupiter (Murray & Dermott 1999). Bodies that have T_j >3.05 are considered to be members of the Centaur class (Gladman et al. 2008) whereas Jupiter family comets have 3> T_J >2(Duncan et al. 2004).

The mean dynamical half-life of Centaurs is ∼2.7 Myr with the vast majority of Centaurs eventually being ejected from the Solar System (Horner et al. 2004) while the Jupiter Family comets have a bit shorter lifetimes of ∼1 Myr (Levison & Duncan 1994). The chaotic evolution of the Centaurs causes a significant number (around one third) to become Jupiter Family Comets at some point in their lifetimes, prior to their eventual ejection from the Solar system such as the Centaur Chiron which has transitioned between the Centaur and Jupiter family comet dynamical classes (Horner et al. 2004). Some can even be temporarily captured as satellites of the giant planets, or to the Jovian and Neptunian Trojan populations (e.g., Horner & Evans 2006; Horner & Lykawka 2012).

Another example of a Centaur recently in the stage of transferring into becoming a Jupiter Family Comet is 29P/Schwassmann-Wachmann, and is located in a region of orbital parameters space with 5.5 au $< q <$8.0 au, and aphelion, 5 au $< Q <$ 7 au that acts as a “gateway” that the Centaurs preferentially inhabit whilst in the process of dynamically transferring to become Jupiter family comets to becoming Jupiter family comets (Sarid et al. 2019) as well as the recently outbursting Centaur Echelclus (Kareta et al. 2019).

The recently discovered Jupiter co-orbital comet P/2019 LD_2 (Sato et al. 2020), with a semi-major axis of 5.30 au, a perihelion of 4.57 au and aphelion of 6.02, may be another example of an object in the transition region between Centaur objects and Jupiter family comets. Initially reported as an inactive object by the ATLAS survey (Tonry 2011) in 2019 June and designated by the Minor Planet Center as 2019 LD_2[1], it was discovered to be active by amateur astronomers[2] and in pre-discovery images taken by ATLAS and in follow-up images of the comet taken by ground-based telescopes resulting in it being given the cometary designation P/2019 LD_2 (Fitzsimmons et al. 2020). Some Centaurs and Jupiter family comets have been observed to have co-orbits with Jupiter and become temporarily captured as Jupiter Trojans (Horner & Evans 2006), though such captures are typically relatively short lived. P/2019 LD_2 is likely to be one such object - whilst technically its orbital elements resemble those of a Jovian Trojan, it is inherently unstable (Hsieh et al. 2021), in stark contrast to the orbits of true Jovian Trojans, which are stable on timescales comparable to the age of the Solar system (e.g., Marzari et al. 2002), having most likely been captured as a result of Jupiter’s migration during the Solar system’s formation, 4.5 Gyr ago (e.g., Morbidelli et al. 2005; Roig & Nesvorný 2015).

---

[1] `https://minorplanetcenter.net/db_search/show_object?utf8=%E2%9C%93&object_id=P%2F2019+LD2`

[2] `http://aerith.net/comet/catalog/2019LD2/2019LD2.html`

One proposed origin for P/2019 LD_2 is that it is a Jupiter family comet in the transition region in orbital parameters space inhabited by objects that are in transition between Centaurs and Jupiter family comets (Steckloff et al. 2020). As comets transfer between becoming denizens of the inner Solar System as short-period, Jupiter Family comets from their origins in the outer Solar System beyond the orbit of Neptune, they will experience a dramatic shift in the thermal environment due to increased thermal insolation from the Sun (De Sanctis et al. 2000; Sarid & Prialnik 2009). The consequence of the increased Solar insolation as the comet nears the Sun is the increased heating and sublimation of volatiles such as CO and H_2O near the comet's surface (Meech & Svoren 2004; Lisse et al. 2020). Another consequence of the increased heating from closer proximity of the Sun is that large-scale ablation of the comet's structure due to thermal stress can occur resulting in it becoming partially or completely disrupted (Fernández 2009). Since P/2019 LD_2 is now in transition between the Centaur and Jupiter Family Comet populations, it seems likely that it has become active for the first time, and as such, that its activity will be rapidly evolving in response to the new epoch of increased Solar heating.

We therefore present in this paper the analysis of visible light high-resolution *Hubble Space Telescope*/Wide Field Camera 3 (*HST*/WFC3 Dressel 2012) observations of P/2019 LD_2 using the approach of Jewitt et al. (2014) and Bolin & Lisse (2020) to understand the dust coma, nucleus properties and constrain its cause of P/2019 LD_2's activity. We will also use mid-infrared (MIR) P/2019 LD_2 observations taken with *Spitzer Space Telescope*/Infrared Array Camera (*Spitzer*/IRAC Werner et al. 2004) combined with the analysis techniques of Reach et al. (2013) and Lisse et al. (2020) to place upper limits on the comet's CO+CO_2 gas production. We also use multi-wavelength observations covering the visible and MIR by building on the techniques of Bolin et al. (2020a) by using a network of ground-based observatories to characterize the physical properties of a transitioning Centaur. In addition, we will examine the long-term orbital properties of P/2019 LD_2 using its latest orbital solution in order to better understand its possible origins and future dynamical evolution.

2. OBSERVATIONS

Observations of P/2019 LD_2 were obtained before the official announcement of its activity in 2020 May both by targeted observations by ground and space-based observatories and serendipitously in the survey observations by the Zwicky Transient Facility (ZTF) (Graham et al. 2019). The time span of our targeted observations is 2019 Sep 7 UTC to 2020 Aug 19 UTC including observations by the Astrophysical Research Consortium 3.5 m telescope (ARC 3.5 m) *Spitzer*, *HST*, Keck I and members of the GROWTH network (Kasliwal et al. 2019) such as Mount Laguna Observatory 40-inch Telescope (MLO 1.0-m), Liverpool Telescope (LT), Lulin Optical Telescope (LOT). A list of our targeted observations and their viewing geometry is listed in Table 1. The time span of our serendipitous observations of P/2019 LD_2 made with the ZTF survey is between 2019 April 9 UTC and 2019 Nov 8 UTC and are listed with their viewing geometry in Table 2.

2.1. *Zwicky Transient Facility*

We searched for serendipitous observations of P/2019 LD_2 made with the Zwicky Transient Facility survey mounted on the Palomar Observatory's 48-inch telescope (Bellm et al. 2019) in the ZTF archive (Masci et al. 2019). The ZTF archive possessed observations of P/2019 LD_2 made as far back as 2019 April 9 UTC which we include up to 2019 Nov 8 UTC. The observations were made in g and r band in images consisting of 30 s exposures. Seeing conditions were typically between

1.5-2.5$''$ and at air masses ranging from 1.4 to 2.6. A full list of observations of P/2019 LD$_2$ made by ZTF containing the viewing geometry and observing conditions is presented in Table 2.

2.2. *Apache Point Astrophysical Research Consortium 3.5 m*

Following the announcement of the appearance of activity of P/2019 LD$_2$[3] (then called 2019 LD$_2$), we triggered target of opportunity observations with the ARC 3.5 M at Apache Point Observatory on 2019 September 7 UTC using the ARCTIC large-format optical CCD camera (Huehnerhoff et al. 2016). The camera was used in full-frame, quad amplifier readout, 2×2 binning mode resulting in a pixel scale of 0.228$''$ and used with the g and r filters. In total, 14 g and r exposures were obtained, each 120 s long and in alternating order between the g and r filters. The telescope was tracked at the sky-motion rate of the comet of 8.6$''$/h. The seeing was 1.4$''$ and the airmass was 1.8 during the observations.

2.3. *Spitzer Space Telescope*

Observations of P/2019 LD$_2$ were made with the *Spitzer Space Telescope* (*Spitzer*) using the IRAC instrument (Fazio et al. 2004) on 2020 January 25-26 UTC (DDT program 14331, PI Bolin et al. 2019a). The observations consisted of 11 Astronomical Observing Requests (AORs) were used, each consisting of 80 x 12 s dithered frames and having a ∼0.44 h duration for a total of 4.8 h clock time. The frames where dithered in groups of 10, with each using a large cycling pattern. The sky at the location of P/2019 LD$_2$ during the *Spitzer* observations possessed a high density of stars due to its low, -18° galactic latitude, therefore shadow observations were used to improve the sensitivity of the observations. Out of a total of 11 AORs, eight were focused on observed P/2019 LD$_2$ for a total of 2.13 h on source time. The remaining three AORs were Shadow observations that were evenly spaced in the sky location covering the trajectory of P/2019 LD$_2$ between 2020 January 02:23:32-23:10:44 that P/2019 LD$_2$ was being observed. The target was centered in the 4.5 μm channel since this channel is sensitive to CO/CO$_2$ emission and also because the object was expected to be brightest at this wavelength. The 4.5 μm IRAC channel has a spatial resolution of 1.2$''$/pixel. The data were reduced in a method as described in (Fernández et al. 2013).

2.4. *Hubble Space Telescope*

The *Hubble Space Telescope* (*HST*) was used to observe P/2019 LD$_2$ with General Observer's (GO) time on 2020 April 1 UTC (HST GO 16077, PI Bolin et al. 2019b). During the one orbit visit, five 380 s F350LP filter exposures were obtained with the UVIS2 array of the WFC3/UVIS camera (Dressel 2012) for a total of 1900 s integration time over a single orbit. The F350LP filter has a central wavelength of 582 nm with a FWHM bandpass of 490 nm (Deustua et al. 2017). The instrument and filter combination of WFC3 and the F350LP filter provides a per-pixel resolution of 0.04$''$ corresponding to 145 km at the topo-centric distance of the comet. The comet was tracked non-sidereally according to its skyplane rate of motion of 40$''$/h.

2.5. *Mount Laguna Observatory 40-inch Telescope*

Multi-band optical images of P/2019 LD$_2$ were obtained with the 1.0 m Telescope at the Mount Laguna Observatory (Smith & Nelson 1969) on 2020 May 17 UTC. Johnson-Cousins B, V and R

---

[3] `http://aerith.net/comet/catalog/2019LD2/2019LD2.html`

filters were used in combination with the E2V 42-40 CCD Camera to obtain 7-9 120 s exposures in each filter. The seeing conditions were 1.92″, the airmass was 1.49 and sidereal tracking was used. This facility is a member of the GROWTH collaboration.

2.6. *Liverpool Telescope*

Observations of P/2019 LD_2 were made in g, r, i and z filters by the 2 m Liverpool Telescope located at the Observatorio del Roque de los Muchachos on 2020 May 29 UTC. The IO:O wide-field camera was used with a 2x2 binning providing a pixel scale of 0.3″ (Steele et al. 2004). Two 30 s exposures were made per filter with the telescope tracking at the sidereal rate. The seeing conditions were 1.21 ″ and the airmass was 1.75. Detrending of data was performed using the automated IO:O pipeline software. This facility is a member of the GROWTH collaboration.

2.7. *Lulin Optical Telescope*

Multiband B, V, and R imaging of P/2019 LD_2 were made by the 1 m Lulin Optical Telescope on 2020 June 23-27 UTC and 2020 July 10 UTC. The observations were made using the 2K × 2K SOPHIA camera with a pixel scale of 0.52 ″(Kinoshita et al. 2005). Exposure times of 90 s were where the telescope was tracked at the non-sideral rate determined by the ephemeris of the comet. The seeing conditions of the observations were ∼1.5″ and the airmass was ∼1.15.

2.8. *Keck I Telescope*

A spectrum of P/2019 LD_2 was obtained using the Low-Resolution Imaging Spectrometer (LRIS) Oke et al. (1995) on the Keck I telescope on 2020 August 19 UTC (PI J. von Roestel, C272). The blue camera consisting of a 2 x 2K x 4K Marconi CCD array was used with the red camera consisting of a science grade Lawrence Berkeley National Laboratory 2K x 4K CCD array. Both cameras have a spatial resolution of 0.135 ″/pixel. The 560 nm dichroic with ∼50% transmission efficiency in combination with the 600/4000 grism for the blue camera, rebinned twice in both the spectral and spatial direction, and the 600/7500 grating for the red camera, rebinned once in the spectral direction and twice in the spatial direction, providing a spectral resolution of 0.8 nm and 0.5 nm, respectively, and a spatial resolution of 0.27″. A total integration time of 300 s was used for the exposure and was obtained at airmass 1.8 in 0.85″ seeing conditions. Both telluric correction and Solar-analog stars were observed at similar air masses as P/2019 LD_2. Wavelength calibration was completed using the HgCdZn lamps for the blue camera and the ArNeXe lamps for the red camera. We used a local Solar analog star to remove the Solar component from the spectrum of P/2019 LD_2. The LPipe spectroscopy reduction package was used to reduce the data (Perley 2019).

3. RESULTS

3.1. *Morphology and nucleus*

Serendipitous pre-discovery observations of P/2019 LD_2 were obtained with ZTF on 2019 April 26 UTC consisting of three 30 s exposures in r band. These pre-discovery data of P/2019 LD_2 have been co-added into a composite image with an equivalent 90 s integration time presented in the top left panel of Fig. 1. The comet has an extended appearance with a ∼20″ long tail with a position angle of ∼260° in the anti-Solar direction. ZTF contained pre-discovery detections of P/2019 LD_2 on 2019 April 9,15 and 20, but the comet did not have a discernible extended appearance in these data.

On 2019 September 7 UTC, the ARC 3.5 m was used to obtain 20 x 120 s exposures of P/2019 LD_2 in r band. A composite median stack with an equivalent exposure time of 2400 s is presented in the top right panel of Fig. 1. In the ARC 3.5 m images, the comet has a diffuse, non-stellar appearance. The tail is not easily defined in the ARC 3.5 m median stack, though the comet's extended appearance is enhanced in the opposite direction of the comet's orbital motion with a position angle of ∼230° and length of 5″.

The center panel of Fig. 1 present the appearance of P/2019 LD_2 in a median stack of five 380 s F350LP image with an equivalent integration time of 1900 s taken with *HST*/WFC3 on 2020 April 01 UTC. Cosmic rays have been removed from the composite image stack with median interpolation of the surrounding pixels. The high-resolution composite *HST* stack were taken when the comet was at an orbit-plane angle of ∼-0.44° and has a tail with a length of ∼32″ limited by background structure caused by galaxies and sky noise opposite of the Solar direction with a position angle of ∼250°. The ∼32″-long tail translates into a length of 6.2×10^8 m given its topo-centric distance of 5.02 au and a phase angle of 10.7°. An enhanced version of the *HST* median composite stack normalized by the distance from the optocenter reveals a possible jet structure ∼1″ long as seen in the bottom panel of Fig. 1. We will discuss the implications of the comet's morphology from these observations on its dust properties below in Section 3.3.

We compare the surface brightness profile of P/2019 LD_2 to the simulated surface brightness profile of a G2 field star WFC3 point-spread function (PSF) assuming the use of the F350LP filter using the TinyTim software (Krist et al. 2011) as seen in Fig. 2. Both the radial profiles of P/2019 LD_2 and the simulated stellar G2V source are computed by azimuthally averaging concentric apertures centered on the optocenter separated by the pixel scale allowed by WFC3 using the F350LP filter. The normalized surface brightness profile of P/2019 LD_2 between 0.24″-1.2″ was fit the functional form was fit to $\Sigma \propto \theta^m$ where Σ is the surface brightness and θ is the distance from the optocenter in pixels resulting in a radial profile slope of m∼-1.71. We note that the radial profile slope is steeper than the typical -1 to -1.5 radial profile slope of comets with an isotopic coma in a steady state (Jewitt & Meech 1987). The steeper m of P/2019 LD_2 may be an independent indication that the comet's dust production rate has changed recently before these observations.

The fitted 0.24″-1.2″ radial profile of P/2019 LD_2 was convolved with the synthetic G2V PSF and subtracted from the measured radial profile of P/2019 LD_2 to calculate a equivalent nucleus brightness of V = 22.6±0.04 assuming a m_V-m_{F350LP}∼0.1(Bolin et al. 2020b). We assume the following phase function for determining the absolute magnitude of the nucleus, H

$$H = V - 5\log_{10}(r_h\Delta) - \Phi(\alpha) \tag{2}$$

where r_h and Δ, α are the heliocentric, topo-centric distance and phase angle of the comet as listed in Table 1 for the 2020 April . $\Phi(\alpha) = 0.04\alpha$, where we assume a phase coefficient of 0.04 in magnitudes/degree, resulting in $H = 15.53\pm0.05$. The true phase coefficient of P/2019 LD_2 is unknown, therefore our uncertainty on the measured value of H is considered a lower limit.

From our measured value of H, we calculate the light scattering cross-section, C, of P/2019 LD_2 in km^2 using the following function

$$C = 1.5\times10^6\, p_v^{-1}\, 10^{-0.4H} \tag{3}$$

where p_v is the albedo the nucleus, assumed to be ∼0.08, the typical albedo measured for Centaurs (Bauer et al. 2013), resulting in C=11.15±0.42 km^2. Converting our measured cross-section to a

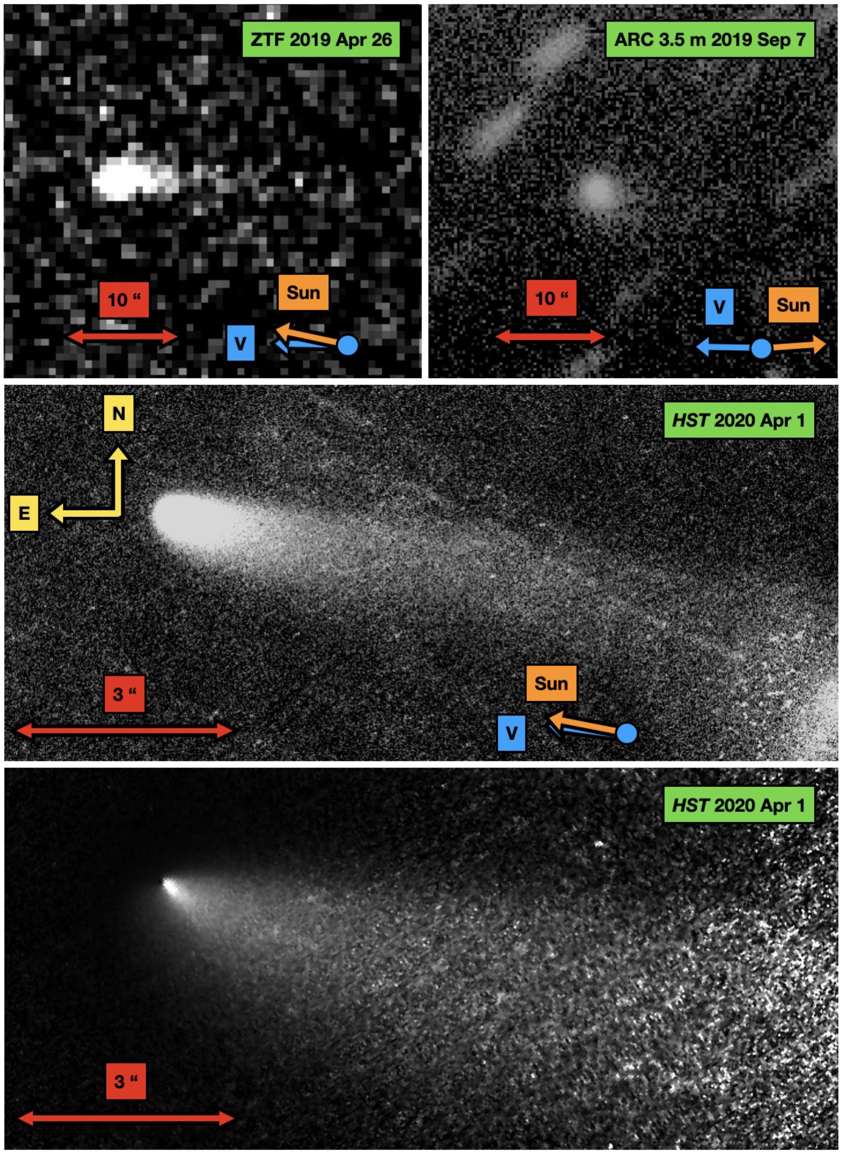

Figure 1. Top left panel: a 90 s equivalent exposure time stack of 3 x 30 s r filter images of P/2019 LD$_2$ taken by ZTF on 2019 April 26 UTC. The image stack was compiled using the ZChecker software (Kelley et al. 2019). The pixel scale is $1''$ /pixel and the seeing was $\sim 2.2''$. An arrow indicating the width of $10''$ is shown for scale, equivalent to ∼30,000 km at the geocentric distance of 4.15 au of the comet on 2020 April 26 UTC. The solar, orbital velocity and cardinal directions are indicated. Top right panel: a 2,400 s equivalent exposure time robust mean stack of 20 x 120 s r filter images of P/2019 LD$_2$ taken with the ARC 3.5 m on 2019 September 7 UTC. The telescope was tracked the comet's motion. The pixel scale is $0.228''$/pixel and the seeing was $\sim 1.4''$. An arrow indicating the width of $10''$ is shown for scale, equivalent to ∼31,000 km at the geocentric distance of 4.28 au of the comet on 2020 September 7 UTC. Center panel: a 1,900 s equivalent exposure time robust mean stack of 5 x 380 s F350LP filter images of P/2019 LD$_2$ taken with *HST*/WFC3 on 2020 April 1 UTC. The pixel scale is $0.04''$/pixel. An arrow indicating the width of $3''$ is shown for scale, equivalent to ∼11,000 km at the geocentric distance of 5.02 au of the comet on 2020 April 1 UTC. Bottom panel: the same as the center panel but normalized according to the radial profile of the comet. A $\sim 1''$ jet-like structure is seen with a position angle of $\sim 210°$.

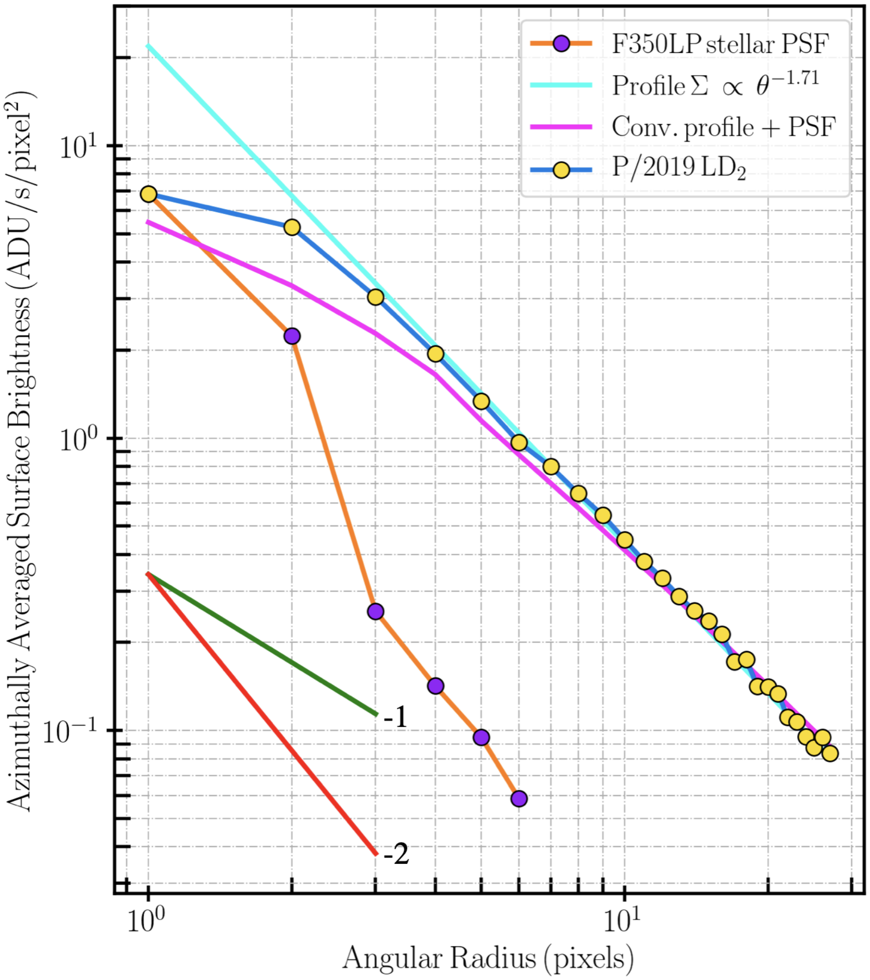

Figure 2. The normalized surface brightness profile of P/2019 LD$_2$ taken with *HST*/WFC3 on 2020 April 1 UTC presented as the yellow circles with a connecting blue line. A surface brightness profile of $\Sigma \propto \theta^{-1.71}$ fitted to the profile of P/2019 LD$_2$ between $0.24''$ and $1.20''$ is plotted as the cyan line. The normalized surface brightness profile of a F350LP stellar PSF assuming a G2V-like source generated using TinyTim (Krist et al. 2011) is plotted as purple circles with a connecting orange line. The surface brightness profile resulting from the convolution of the F350LP stellar PSF and the fitted $\Sigma \propto \theta^{-1.71}$ surface brightness profile of P/2019 LD$_2$ is plotted as a pink line. Logarithmic Surface brightness gradients with m = -1 and m = -2 are plotted as green and red lines respectively for comparison. Statistical error bars on the surface brightness computed assuming Poissonian statistics at each radius element are smaller than the plot symbols used for both P/2019 LD$_2$ and the synthetic stellar PSF.

radius using $r = (C/\pi)^2$, we obtain a radius of $\sim$1.8 km, comparable to the radius estimates of P/2019 LD$_2$ based on un-resolved photometry of P/2019 LD$_2$ based and on the non-detection of P/2019 LD$_2$ in ground-based pre-discovery imaging of the comet (Schambeau et al. 2020). We note that this is a radius estimate based on a single observation and represents a size assuming a spheroid shape. Significant deviations from a spheroid shape such as a bi-lobal (Nesvorný et al. 2018) or elongated shape (Bolin et al. 2018; Hanuš et al. 2018) as has been observed for other comet-like bodies may require additional observations to be made of P/2019 LD$_2$ to accurately determine its size.

3.2. *Photometry, lightcurve and spectrum*

Using the combination of our ground-based observations with the ARC 3.5 m taken on 2019 September 7 UTC, the MLO 1.0-m on 2020 May 27 UTC, the LT on 2020 May 29 UTC and Lulin Optical Observatory on 2020 July 10 UTC, we have calculated the mean colors of P/2019 LD_2 using 10,000 km photometric apertures of g-r = 0.60±0.03, r-i=0.18±0.05, i-z=0.01±0.07. The filter configuration and viewing geometry of our observations are presented in Table 1. The equivalent angular size of the 10,000 km used in our photometric calculations ranged from 3.2″ to 3.7″ with the seeing during observations ranging from 1.2″ to 1.9″. Color transformations were used from Jordi et al. (2006) to convert the photometric colors measured in BVR Johnson-Cousins filters measured with photometry of P/2019 LD_2 from the MLO 1.0-m and LT to the SDSS system.

Our visible measured colors of P/2019 LD_2 are reddish to neutral in the ∼480 nm to ∼910 n wavelength range covered by our filters consistent with the measured colors of other active Solar System comets as presented in Fig. 3. For comparison purposes only, we have included the colors of inactive objects in Fig 3. We note that the measured colors of P/2019 LD_2 from our observations are somewhat bluer compared to the colors of active and inactive Centaurs measured by Jewitt (2015), though this may be due to the longer wavelength coverage of our observations which go as far as ∼910 nm compared to the shorter visible-wavelength observations of Jewitt (2015).

Images from each of the *Spitzer* DDT program 14331 AORs 1,4,6,9 and 10 that were used to take images of P/2019 LD_2 from 2020 January 25 2:23 to 23:11 UTC were reduced using the reduction methods described in Fernández et al. (2013). Images obtained during each of these five AORs using the 4.5 μm channel were co-added to form a single composite image with an equivalent exposure time of 948 s for each AOR.

P/2019 LD_2 was located in a crowded star field at a galactic latitude of ∼-18°. Therefore, due to the imperfections in the shadowing technique, we used an aperture size with an angular width of 3.24″ equivalent to 10,000 km at the topo-centric distance of 4.26 au of the comet from *Spitzer*. We obtain an on-source flux density for P/2019 LD_2 of 35.6±2.8 μJy at 4.5 μm using the average of the five photometry measurements from the composite images made from each of the AORs 1, 4, 6, 9 and 10. The comet has a slightly extended appearance of more than ∼2.4 ″ as seen in Fig. 4 and an aperture correction was applied to the flux density measurement. The flux from the nucleus assuming a ∼km-scale nucleus radius as measured in Section 3.1 is ∼0.1 μJy, less than 1% of the total flux.

We present the A$f\rho$ based off of the *Spitzer*/IRAC photometry of P/2019 LD_2 using the A$f\rho$ definition of A'Hearn et al. (1984) which is a quantity in units of length, in this case cm, that corrects the comet's brightness with respect to heliocentric distance, geocentric distance, aperture size, Solar spectrum and filter wavelength. The values A$f\rho$ are normalized to 0° phase angle, $A(0°)f\rho$, using the Halley-Marcus cometary phase function defined by Schleicher & Bair (2011). Assuming that the entirety of the flux in the 4.5 μm *Spitzer*/IRAC observations is from dust in local thermal equilibrium, we calculate a $A(0°)f\rho = 334$ cm. This is a strict upper limit due to the possible If we assume that the entirety of the flux from the comet is from CO emission and that the gas speed is 0.5 km/s, we measure a gas production rate of $1.6{\pm}0.1{\times}10^{27}$mol/s similar to the results of (Woodney et al. 2020). For CO_2, assuming that the entirety of the flux is due to gas emission, we obtain a gas production rate of $1.4{\pm}0.1{\times}10^{26}$mol/s comparable to the CO_2 measured for comets observed in the MIR at similar heliocentric distances (Reach et al. 2013; Bauer et al. 2015).

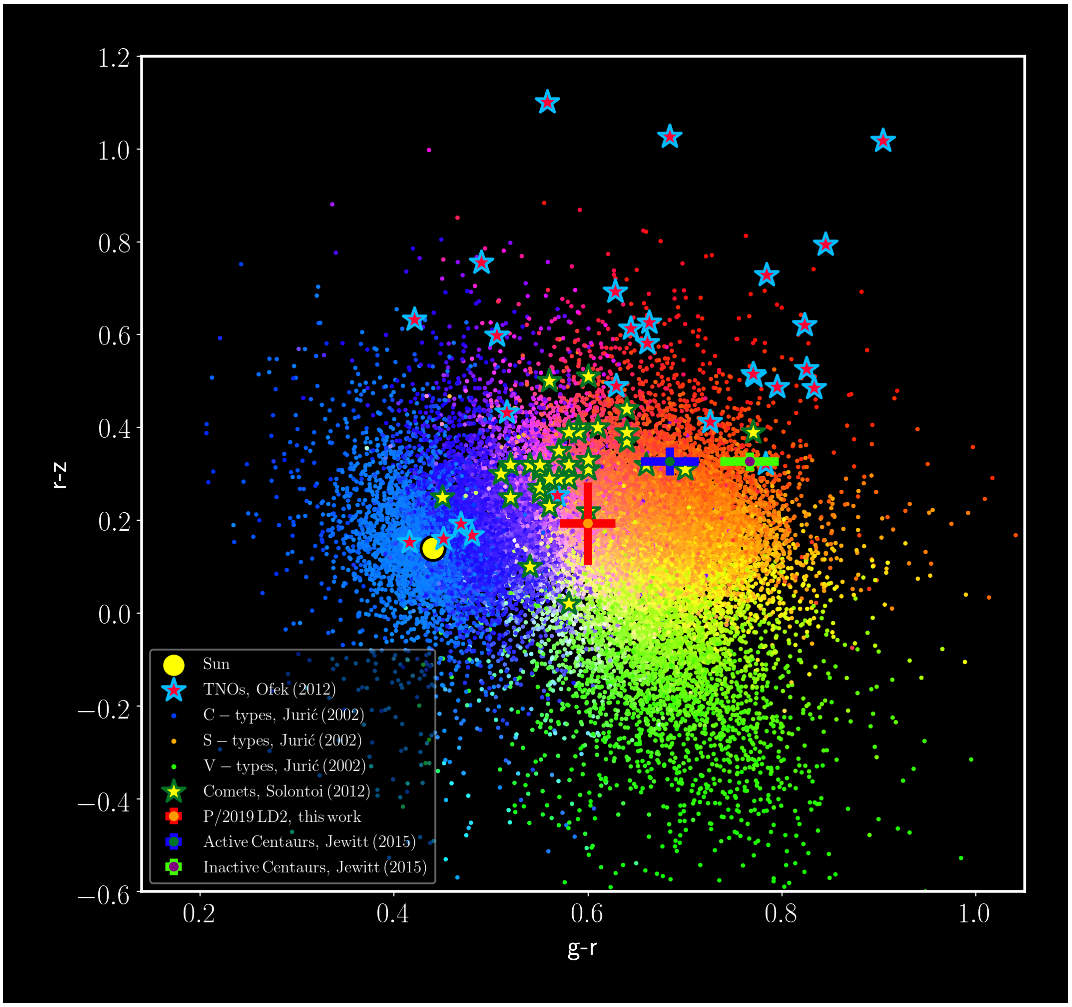

Figure 3. $g-r$ vs. $r-z$ colors of P/2019 LD$_2$ plotted with $g-r$ and $r-z$ colors of inactive Solar System C, S and V-types asteroids (Ivezić et al. 2001; Jurić et al. 2002; DeMeo & Carry 2013), active comets (Solontoi et al. 2012) and Kuiper Belt objects (Ofek 2012). The colorization scheme of data points for asteroids by their *griz* colors is adapted from Ivezić et al. (2002). The colors of active and inactive Centaurs from (Jewitt 2015) is also included. The most appropriate color comparison between the color of P/2019 LD$_2$ and other Solar System bodies is between the active comets in Solontoi et al. (2012) and the active Centaurs from Jewitt (2015) because the colors of P/2019 LD$_2$ are most representative of its dust rather than bare nucleus. The colors of inactive bodies are included for comparison purposes only.

Using our archival observations of P/2019 LD$_2$ from ZTF taken between 2019 April 9 UTC and 2019 November 8 UTC, we have plotted the equivalent r magnitudes of P/2019 LD$_2$ as a function of time since the perihelion date of 2020 April 10 UTC, $(T - T_p)$ measured with equivalent 20,000 km apertures presented in the top panel of Fig. 5 with observational details in Table 2. These observations include data taken in g-band which have been corrected to an equivalent r-band magnitude using our g-r color estimate for P/2019 LD$_2$ of ∼0.6. The 20,000 km aperture was equivalent to an angular size of 5.4″ on 2019 November 8 UTC when the comet had a geocentric distance of 5.14 au and an angular size of 7.52″ when the comet had a geocentric distance of 3.67 au on 2019 July 1 UTC. The measured local seeing in the ZTF images at the time of observation ranged between 1.6″ to 3.9″ with a median seeing value of 2.0″. Using only the r-band photometry, the data show a secular brightening trend of

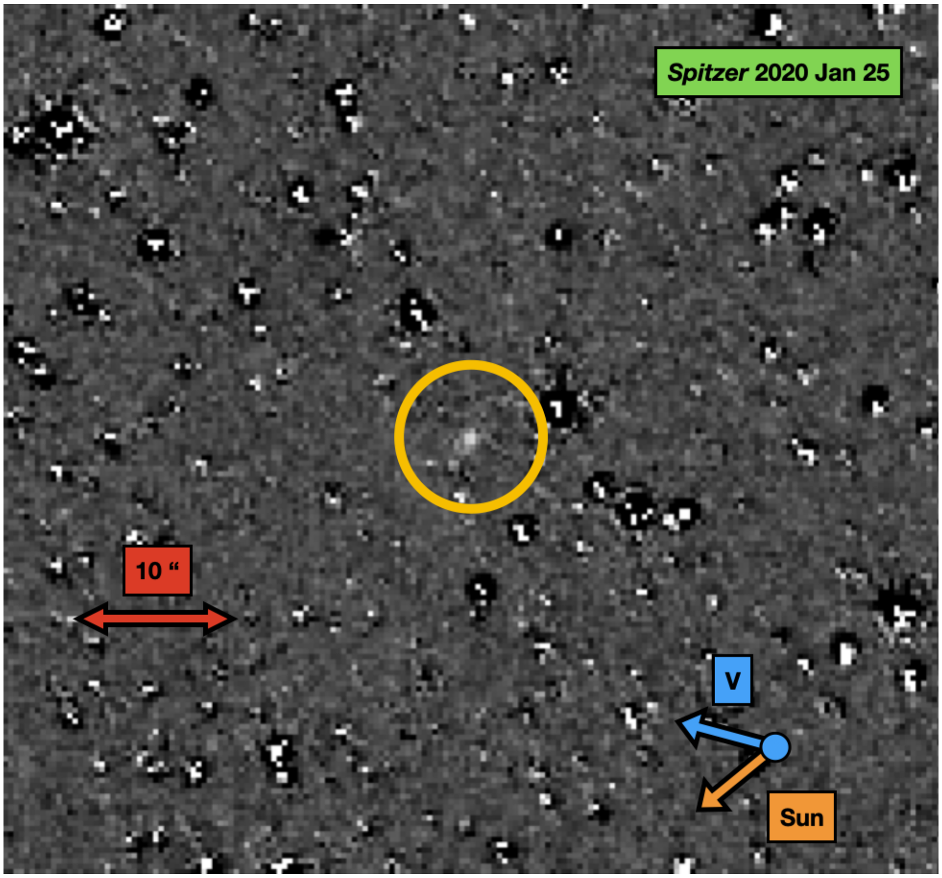

Figure 4. A 948 s equivalent integration time composite image stack made from *Spitzer*/IRAC observations of P/2019 LD_2 taken during *Spitzer* DDT program 14331 AOR 1 on 2020 January 25 02:23:32 UTC. The detection of P/2019 LD_2 has been encircled in yellow. The pixel scale is 1.2″/pixel. An arrow indicating the width of 10″ is shown for scale, equivalent to ~31,000 km at the topo-centric distance of 4.256 au of the comet on 2020 January 25 UTC. The solar, orbital velocity and cardinal directions are indicated.

the comet as the comet approached opposition on 2019 June 24.42 UTC increasing in brightness by $1.6\pm0.2\times10^{-2}$ mags/day. After leaving opposition, the comet showed an asymmetrical secular fading trend of $0.4\pm0.1\times10^{-2}$ mags/day compared to the pre-opposition brightening trend.

In addition to photometry, we present the A$f\rho$ based off of the ZTF photometry of P/2019 LD_2 using as implemented by Mommert et al. (2019). The values A$f\rho$ are normalized to 0° phase angle, $A(0°)f\rho$ and are plotted against the second Y-axis in the top panel of Fig. 5 and presented in Table 2. Values of constant $A(0°)f\rho$ are plotted for reference in the top panel of Fig. 5. The value of $A(0°)f\rho$ rises consistently over the span of our observations resulting in asymmetry in the brightness of P/2019 LD_2 as it passed through opposition on 2019 June 24 UTC ($T - T_p$ = -291 days). Before opposition between $T-T_p$ = -370 and -312, the error weighted mean of $A(0°)f\rho = 93.9\pm11.8$ cm, between $T-T_p$ = -312 and -291, $A(0°)f\rho = 113.1\pm8.57$ cm. After opposition the error weighted mean of $A(0°)f\rho$ between $T - T_p$ = -291 and -211 equaled 136.2±9.7 cm and from $T - T_p$ = -211 and -50, $A(0°)f\rho$ = 188.8±25.8 cm. The range of $A(0°)f\rho$ from 85 cm to 200 cm is consistent with the observe A$f\rho$ range of comets which ranges from 1 to 10,000 cm (A'Hearn et al. 1995).

3.3. *Dust properties and mass loss*

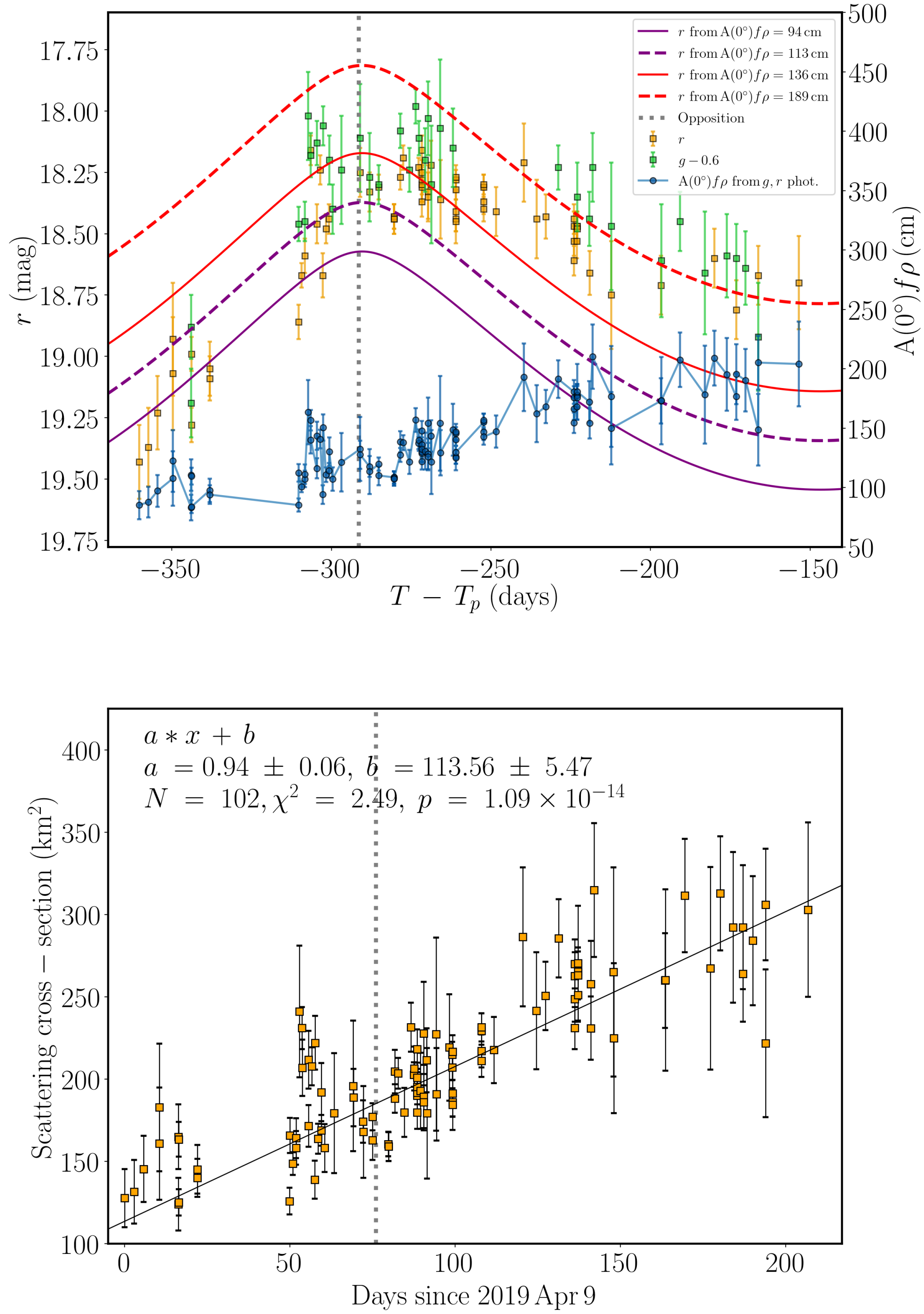

Figure 5. Top panel: g and r band photometric lightcurve of P/2019 LD$_2$ vs. time from perihelion $(T - T_p)$ measured using a fixed 20,000 km aperture between 2019 April 9 UTC and 2019 November 8 UTC using the data from Table 2. Multiple lines of $A(0°)f\rho$ = 94 cm, 113 cm, 136 cm, 189 cm as purple and red solid and dashed lines to reflect the change in the comet's brightness as the comet moved through opposition at $(T - T_p)$ = -291.5 days on 2019 June 24 UTC which is shown as a vertical grey dotted line. In addition, values of $A(0°)f\rho$ calculated using the brightness values and viewing geometry in Table 2 are presented as dark blue data points connected by a light blue solid line. Bottom panel: The scattering cross-section of P/2019 LD$_2$ calculated from Eq. 3 as a function of days since 2019 April 09 UTC from the photometric data presented in Table 2. The black line shows the minimized χ^2 fit to the cross-section measurements and the vertical dash-dot line corresponds to the date when P/2019 LD$_2$ was at opposition on 2019 June 24 UTC.

In addition to calculating the $A(0°)f\rho$ of P/2019 LD_2, we calculate the value of C for each of the equivalent r-band magnitudes in Table 2 using Eqn. 3 which are plotted in the bottom panel of Fig. 5. A linear function is fit to these data resulting in a fitted slope parameter value of dC/dt = 0.94±0.06 km^2/day. The change in phase angle over the time of our observations is modest as seen in Table 2, therefore variations in the phase function used to calculate C should have a minimal effect on the estimate of the uncertainty of our measured slope parameter. Extrapolating backward in time beyond the range of our data results in a $C = 0$ km^2 at ∼135 days before 2019 April 9 UTC, the date of our first photometry data point or on 2018 November 24 UTC during which P/2019 LD_2 had a heliocentric distance of ∼4.8 au when water ice begins to sublimate (Lisse et al. 2019).

The dimensionless ratio of Solar radiation and gravitational forces is defined by β (Burns et al. 1979)

$$\beta = \frac{2L_0 r_H^2}{g_\odot(1\text{au})t^2} \tag{4}$$

where L_0 is the length of dust travel, in this case, the observed length of the tail of P/2019 LD_2 of 6.2×10^8 m, r_H is the heliocentric distance, $g_\odot(1\text{au})$ is the gravitational acceleration of towards the Sun at 1 au equal to 6.0×10^{-3} m/s^2 and t is the time of particle release. Assuming a mean value of r_H∼4.6 au, $L_0 = 6.2\times10^8$ m, the length of the tail estimated from the 2020 April 1 UTC *HST*/WFC3 images, and $t = 4.3\times10^7$ s, the time between the 2020 April 1 UTC *HST*/WFC3 observations and the estimated start of the activity, we calculate a value of β=2.4×10^3. Making the assumption that the dust particles are dielectric spheres (Bohren & Huffman 1983), the reciprocal of our estimated value of β translates into particle size, $\bar{a}$, in μm of ∼400 μm. However, we caution that this may be a lower limit due to the limitations of our tail length measurement by the contamination of background galaxies in the *HST*/WFC3 images due to variations in the activity of P/2019 LD_2 affecting our estimate of t based on the backwards extrapolation of the photometric data.

Assuming our estimated particle size of ∼400 μm, we estimate the total mass loss over the duration of our ZTF observations between 2019 April 9 UTC and 2019 November 8 UTC by $M = 4/3\rho\bar{a}\Delta C$ where ΔC is the difference between the cross section at the start and end of our observations equal to 220 km^2. Assuming a dust density of 1 kg/m^3 (McDonnell et al. 1986), we obtain a total mass loss over the time span of our observations of ∼10^8 kg. Adopting our estimated value of dC/dt ∼1 km^2/day, we obtain a mass loss rate using $\dot{M}$=$4/3\rho\bar{a}$ dC/dt∼5×10^5kg/day.

To estimate the fraction of active area of P/2019 LD_2, A, we take the ratio between the mass-loss rate and the equilibrium mass sublimation flux at 4.6 au, $f_s = 1.4\times10^{-5}$ kg m^{-2} (Jewitt et al. 2015) where A∼0.4 km^2. Thus, ∼10% of P/2019 LD_2's surface is active assuming our inferred size radius of 1.8 km from Section 3.1. An alternative assumption is to assume that P/2019 LD_2 has a 100% active area setting a lower limit to its radius of 0.2 km.

In addition, we use the perpendicular profile of P/2019 LD_2 taken with the high-resolution images from *HST*/WFC3 to estimate the out-of-plane distribution of dust with a minimum of projection effects as the Earth passed through the projected orbital plane of P/2019 LD_2 with a projected orbital plane angle of only 0.4° on 2020 April 1 UTC. We measured the FWHM along the perpendicular direction of the tail's profile as a function of distance from the optocenter, ℓ_T between 0 and ∼2″ in increments of 0.12″ slices as are plotted in Fig. 6.

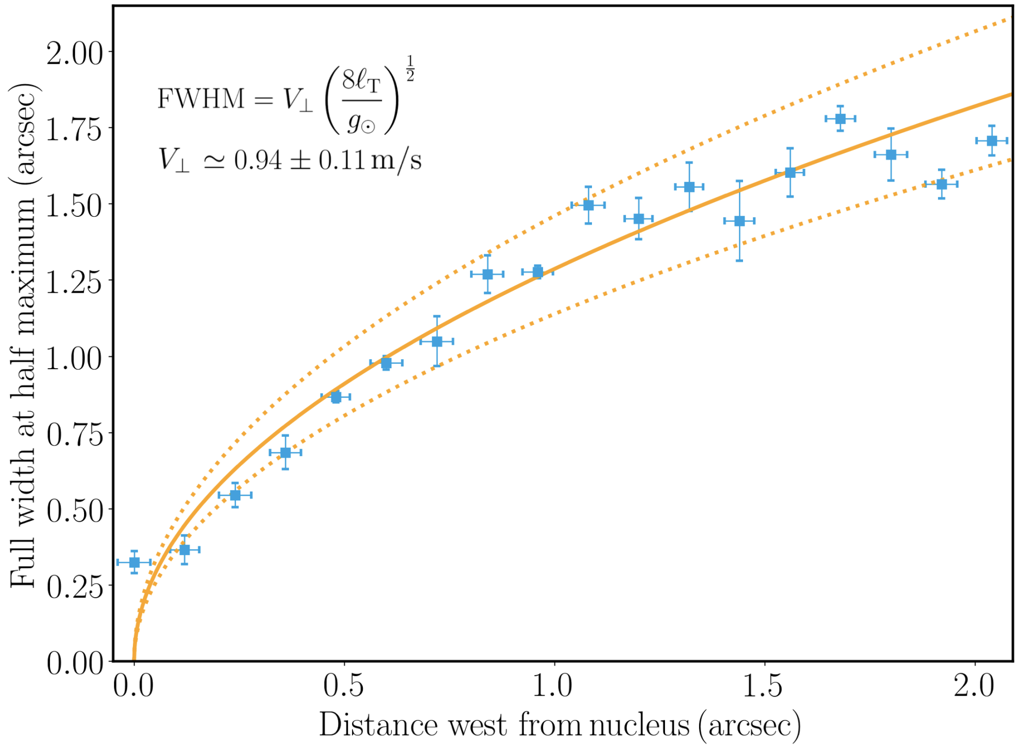

Figure 6. The FWHM of the dust tail of P/2019 LD$_2$ vs. the westward angular distance, ℓ_T, from the nucleus optocenter of P/2019 LD$_2$ plotted as blue data points when the comet was observed at a -0.44° topo-centric and target orbital plane angle with *HST*/WFC3 on 2020 April 1 UTC. The best fit line in ℓ_T vs. FWHM space according to Eq. 5 with $V_\perp$ = 0.94±0.11 m/s is plotted as an orange line.

Neglecting projection effects, FWHM of the tail gradually widened with ℓ_T and was fit to the following function

$$\mathrm{FWHM} = V_\perp \left(\frac{8\ell_\mathrm{T}}{g_\odot}\right)^{\frac{1}{2}} \tag{5}$$

from (Jewitt et al. 2014) where $V_\perp$ is the component of the ejection velocity perpendicular to the orbital plane, equal to ∼1 m/s. We estimate that the perpendicular component of the ejection velocity scales with $\mathrm{V}_\perp \sim$ 1 m/s $(\bar{a}/\bar{a}_0)^{-1/2}$ where $\bar{a}_0 = 400$ μm (Jewitt et al. 2014).

3.4. *Spectrum*

The spectrum of P/2019 LD$_2$ was extracted using a 7.4″-wide region centered on the peak of the continuum's brightness. We compute the normalized reflectance spectrum of P/2019 LD$_2$ taken with Keck/LRIS on 2020 August 19 UTC in the wavelength range between 400 nm and 1000 nm by dividing the P/2019 LD$_2$ spectrum by our Solar analog spectrum and normalized to unity at 550 nm. The resulting spectrum indicates a reddish to neutral coma color for P/2019 LD$_2$ as seen in Fig. 7 . We measure a slope of ∼16%/100 nm between 480 and 760 nm and a flatter spectrum at between 760 nm and 900 nm consistent with the photometric colors taken by LT on 2020 May 29 plotted over the LRIS spectra in Fig. 7 for reference. Our spectrum shows no sign of C_2 emission in the 505 nm to 522 nm range (Farnham et al. 2000) in the highlighted range in Fig. 7.

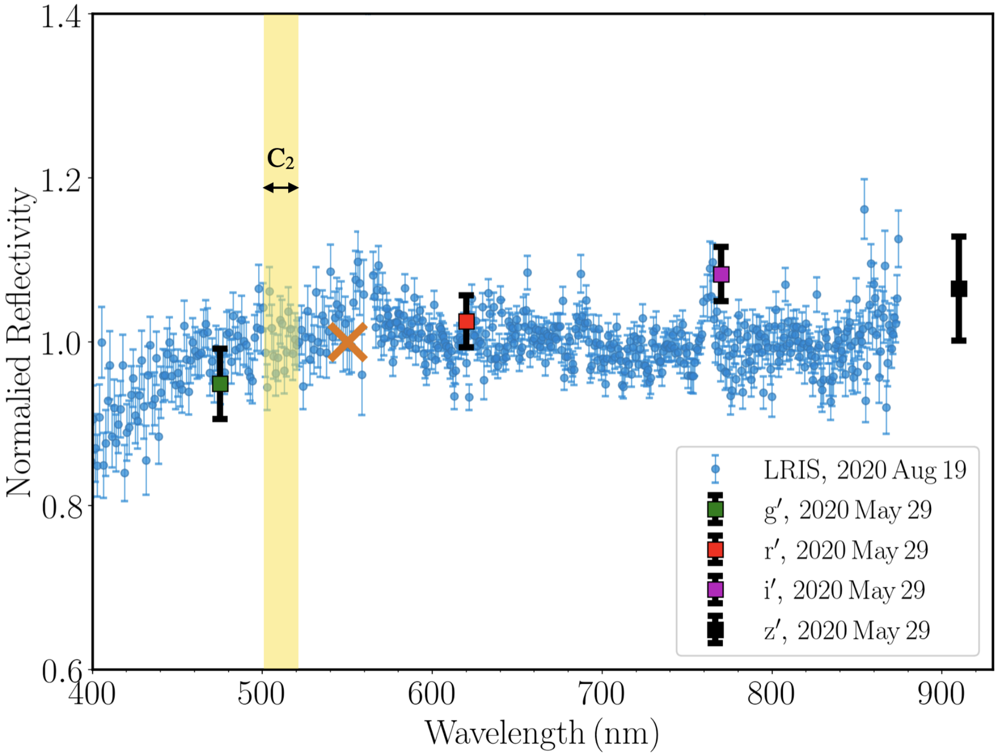

Figure 7. Visible wavelength reflectance spectrum taken of P/2019 LD_2 with the LRIS instrument on Keck I on 2020 August 19 plotted as blue dots. The error bars on the spectrum data points correspond to 1-σ uncertainty. The spectrum has been normalized to unity at 550 nm indicated by the orange cross. The spectrum presented was obtained by combining two spectra from the blue camera using the 600/4000 grism and the red camera using the 600/7500 grating with a 560 nm dichroic Oke et al. (1995); McCarthy et al. (1998). The data have been rebinned and smoothed by a factor of 10 using an error-weighted mean. The spectral range of the cometary C_2 emission line has been indicated by the yellow shaded area (Farnham et al. 2000). The spike in the spectrum at ∼560 nm is due an artifact caused by the dichroic solution and the spike at ∼760 nm is caused by the telluric H_2O absorption feature in both the comet and Solar analog spectrum.

We set an upper limit to the C_2 gas production of P/2019 LD_2 using the mean V-band continuum flux density of P/2019 LD_2 using its measured 550 nm flux, $\text{flux}_V = 1.52{\times}10^{-15}$ erg cm^{-2} s^{-1} nm^{-}1. The 1σ continuum fractional statistical uncertainty of our P/2019 LD_2 spectrum in the range spanning the 505 nm to 522 nm is 0.01 corresponding to a 3σ flux density $\text{flux}_{\text{C}_2} = 2.13{\times}10^{-17}$ erg cm^{-2} s^{-1} nm^{-}1 including a correction of 0.6 for slit losses. The 3σ upper limit to the flux in the 17 nm width of the C_2 band is $F_{\text{C}_2} \leq 3.62{\times}10^{-16}$ erg cm^{-2} s^{-1}. The 3σ upper limit on the number of C_2 molecules projected within the 7.4″ × 1.0″ spectroscopic slit assuming that the coma is optically thin is

$$N_{mol} = \frac{4\pi\Delta^2 F_{\text{C}_2}}{g(r_h)} \tag{6}$$

where $g(r_h)$ is the fluorescence efficiency factor of the C_2 spectral band at r_h where $g(1\,\text{au}) = 2.2{\times}10^{-14}$ erg s^{-}1 radical^{-1} (A'Hearn 1982) which results in $N_{mol} \leq 1.27{\times}10^{27}$ molecules.

We apply the assumptions of the Haser model (Haser 1957) to determine a coarse 3σ upper limit on the production rate of C_2. The Haser model uses two length scales, the "parent" molecule species length scale, L_P, and the "daughter" molecule species length scale, L_D, to described the distribution of the radicals. For C_2 at a r_h of 4.594 au, $L_P = 5.3\times10^5$ km and $L_D = 2.5\times10^6$ km. In addition, we assume the speed of the molecular gas is 0.5 km/s which is used to determine the residence time of the molecules in the projected slit (Combi et al. 2004). Using these assumptions with the Haser model we find the 3σ upper limit to the gas production rate $Q_{C_2} \lesssim 7.5\times10^{24}$ mol/s which is a similar limit compared to the measured Q_{C_2} of other Solar System Comets at similar heliocentric distances (Feldman et al. 2004) and to the results of Licandro et al. (2020). Scaling our measured spectroscopic upper limit on the Q_{C_2} gas production rate to a OH gas production rate using the median ratio of C_2 to hydroxyl production rate for solar system comets (A'Hearn et al. 1995) results in a spectroscopic upper limit to $Q_{OH} \lesssim 2.4\times10^{27}$ mol/s and a mass loss rate in water of $dM_{H_2O}/dt \lesssim 80$ kg/s.

3.5. *Orbital evolution*

In order to investigate the long-term dynamics of 2019 LD_2, we simulated 1000 clones along with the xyz uncertainties, similar to the method used by Holt et al. (2020); Bolin et al. (2020); Steckloff et al. (2020). Orbital six-vectors were generated with uncertainties from the JPL Horizons Orbit Solution dated 2020 May 20 00:43:28 and set for the 2019 September 15 00:00 UTC epoch. In addition, we use the major gravitational components of the Solar system (Sun, Jupiter, Saturn, Uranus and Neptune). The simulations were conducted using `REBOUND` (Rein & Liu 2012) with the hybrid `MERCURIUS` integrator (Rein et al. 2019). We ran two sets of integrations, a short-term set, integrated for 100 years, and a long-term set for 1×10^7 years. For each simulation set, we use a timestep of 0.3954 years. In the short-term integrations (100 years), we use a sample time of the timestep (0.3954 years). For the long-term integrations, we output every 1000 years and analyze the time at which the clones escape the Solar System (distance from Sun larger than 1000 au).

The short-term integrations replicate the previous work of Steckloff et al. (2020) and Hsieh et al. (2021). In the simulations, we find that the clones entered the Jovian region approximately 2.37 years ago, and are ejected from the region 8.70 years in the future (See top left panel of Fig. 8 for a clone example). As was found previously, 2019 LD_2 transitions from a Centaur, with an approximate semi-major axis of 8.6 au to a Jupiter family comet with a semi-major axis of 6.2 au, spending 11.0712 years in the Jovian region (semi-major axis 5.2 au). In the long-term simulations (1×10^7 years) we find that 73.2% of the clones escape the Solar system within the first 1×10^6 years as seen in the bottom-right panel of Fig. 8. Within the first 4.5×10^6 years, 94.74% of the clones are ejected from the Solar system. The remaining 5.3% of clones remain in the Solar system for the 1×10^7 years of the simulations. The decay rate of the clones does not follow any parameterization, unlike Centaurs which have a decay curve allowing calculation of a mean half-life (2.7×10^6 years Horner et al. 2004).

4. DISCUSSION AND CONCLUSIONS

From our observations spanning multiple observatories, transitioning comet P/2019 LD_2 exhibits interesting features in comparison with other short period Solar System comets such as a higher value of A$f\rho$ of 85-200 cm (A'Hearn et al. 1995) at a helio-centric distance between 4.7 and 4.6 au compared to other short period comets at a similar helio-centric distance (Kelley et al. 2013; Ivanova et al. 2014; Bauer et al. 2015) and a ∼km-scale nucleus (Fernández et al. 2013) as well as reddish to neutral color properties (Jewitt 2015). The comet's morphology observed over multiple epochs exhibits the presence of a tail since 2019 April suggesting sustained activity versus an impulsive event as well as having a moderate upper limit for the production of CO/CO_2 of $\sim10^{25}$ mol/s based on our

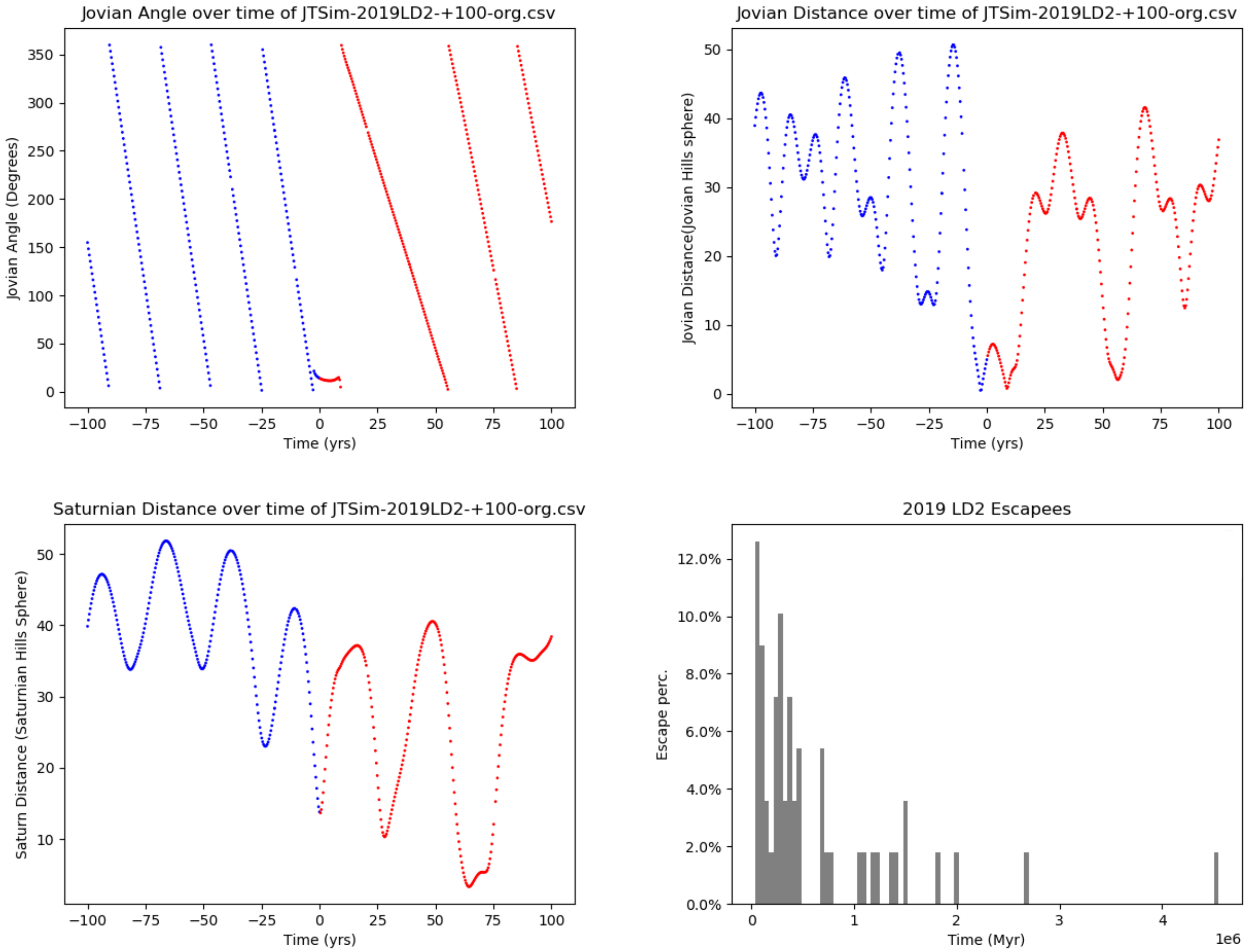

Figure 8. Top left panel: Jovian angle defined as the relative longitude between Jupiter and P/2019 LD_2 as a function of time between -100 and 100 years centered on 2019 September 15 UTC. Except for a brief period of time between -2 and 3 years where the Jovian angle was $\sim$20°, the Jovian angle cycled between 0° and 360°. Top right panel: same as the top left panel except for the Jovian distance defined as the distance between P/2019 LD_2 and Jupiter in Jovian hill spheres ($\sim$0.35 au) as a function of time. The local minimum in the Jovian distance occurred $\sim$2.77 years ago with a distance of $\sim$0.50 Jovian hill radius, or 0.17 au. Bottom left panel: same as the top right panel except for the Saturn distance defined as the distance between P/2019 LD_2 and Saturn in Saturn Hill spheres (0.43 au). The local minimum occurs in $\sim$60 years when P/2019 LD_2 comes within $\sim$3.3 Hill radii or 1.42 au of Saturn. Bottom right panel: the percentage of orbital P/2019 LD_2 clones that have escaped the Solar System (reached >1000 au from the Sun) per bin in duration of time. Each bin is $\sim$50,000 years wide. Within the first million years of the simulation, $\sim$73.2% have escaped the Solar System. By 10 million years, $\sim$95% have escaped the Solar System.

Spitzer observations taken in 2020 January. It is also very active when compared to 29P (although 29P is located at a slightly farther heliocentric distance of $\sim$6 au) on a per unit surface area basis ($Af\rho\sim150\text{cm}/(1.8\text{ km})^2\sim50\text{ cm/km}^2$ for P/2019 LD_2) vs ($Af\rho\sim1000\text{ cm }/(30.5\text{ km})^2\sim1\text{ cm/km}^2$ for for 29P, Ivanova et al. 2011), using the latest value for SW1's size from Schambeau et al. (2019). But this activity seems to produce quite large ($\sim$100 μm) reddish dust particles containing copious amounts of water ice according to our work and that of Woodney et al. (2020).

In addition to the morphology of the comet indicating sustained activity, the activity indicated by the photometry of the comet observed between 2019 April and 2019 November by ZTF activity is consistent with steadily increasing since late 2018 up through the end of 2019 and into 2020 as the comet nears its perihelion on 2020 April 10 UTC. The length of the tail in deep HST imaging as well as our inferred start of activity date of late 2018 implies that the coma consists of $\sim$100 μm-scale dust ejected at a relatively low velocity of $\sim$1 m/s. Although this is roughly consistent with the escape speed of a non-rotating comet nucleus of radius $\sim$1.8 km as inferred by our observations, it is unlikely that the dust is being ejected exclusively by rotational mass shedding suggested by the low ejection velocity (e.g. Ye et al. 2019; Lin et al. 2020) and is being transported by the sublimation of volatiles due to the increased activity of the comet as it nears perihelion or a possible combination of these two effects.

The size of the active region on P/2019 LD_2 of $\sim$0.4 km^2 is too large to explain the low ejection velocity of the dust as for other comets with low dust ejection velocities whose activity is driven by the sublimation of volatiles (Jewitt et al. 2014). Subsequent observations of P/2019 LD_2 to determine the rotation state of the comet will be necessary to understand if it is rotating near its critical rotation limit indicating the role of rotational mass shedding in its activity or if the comet has the possibility of becoming rotationally disrupted in the near future or if it has disrupted in the recent past (Moreno et al. 2017; Vokrouhlický et al. 2017). Given the 4-5 au location of the comet during its recent epoch of activity, the distance at which water ice begins to sublimate (Meech & Svoren 2004), it is likely that the activity is being driven primarily by the sublimation of water ice. An additional possible mechanism may be the transformation of amorphous water ice into crystalline water as has been suggested before as an activity-driving mechanism for Centaurs (Jewitt 2009). It is possible for other volatiles such CO to partially drive the activity of P/2019 LD_2 as seen in other distant comets (e.g., Bolin et al. 2020b) and 29P (Gunnarsson et al. 2008), however the lack of detection of the activity at large heliocentric distances (Schambeau et al. 2020) seems to suggest that hyper-volatiles are not the dominant drivers of the activity of P/2019 LD_2. If the lack of hyper-volatiles driving the activity of P/2019 LD_2 is confirmed, it may suggest that P/2019 LD_2 has spent a significant amount of time as a Centaur within 15 au of the Sun (Horner et al. 2004) where these hyper-volatiles may have had a greater chance to become completed compared to water ice which is non-volatile at that distance.

P/2019 LD_2 is beginning to enter the region where water ice begins to sublimate appreciably. Not at high rates, but enough so that a patch of pure water ice in the surface would disappear on year-long timescales (Lisse et al. 2020). The beginnings of Mobilization of water ice for a weakly structured surface such as found on 67P (O'Rourke et al. 2020) which could lead to the slow flaking off of large chunks of the loosest, weakest material that had never felt such stresses before. In this scenario gas is evolved in order to drive dust off the object - but not much gas, so that it is hard to detect its presence, and the material driven off should be water ice rich, as this ice is the last, most refractory ice expected in a cometary body before it is totally volatile ice depleted. If this is the case, then we may expect to see P/2019 LD_2's activity modulated by its motion towards/away from the Sun over an orbit. Much like the MBC's/AA's activity is modulated as they travel inside/outside the 2.5 au water "ice line" where water ice boils furiously into vacuum (Hsieh et al. 2015a,b), P/2019 LD_2's activity could be modulated by its traversing the water ice turn on line of activity. Future monitoring observations over the next years will determine if this is the case, as is suggested by the smoothly increasing A$f\rho$ towards perihelion values we find for P/2019 LD$_2$, they do not appear to be describing an impulsive outburst.

In our long-term simulations (1×10^7 years), we show the temporary nature of 2019 LD$_2$. The up to 94.7% of the clones escape the solar system within 4.5×10^6 years, with 73.2% escaping in the first 1×10^6 years. This is shorter than the mean half-life of Centaurs of 2.7×10^6 years (Horner et al. 2004), comparable to the lifetime of more unstable Trojans such as 1996 AR$_{20}$ (halflife ∼540 kyr) and 2000 EC$_{98}$ (610 kyr) of that same work. These simulations, along with the works of Steckloff et al. (2020) and Hsieh et al. (2021), highlight the importance of 2019 LD$_2$ as an object transitioning between two populations. Without a robust assessment of survey selection effects (e.g., Jedicke et al. 2016; Boe et al. 2019) it is difficult to assess the true population of comets in a temporary co-orbital configuration with Jupiter and transitioning between the Centaur and Jupiter family comet populations (Sarid et al. 2019). However, we can use our estimated size of P/2019 LD$_2$ in comparison with the population estimates of Centaurs in the transition region (Steckloff et al. 2020). Steckloff et al. (2020) predict that there are ∼40-1,000 objects in the transition region with radius >1-3 km with fewer if cometary fading is considered in the population estimate (Brasser & Wang 2015). Using these transition object population estimates and our estimate of the radius of P/2019 LD$_2$ of ∼1.8 km suggests there are ∼100 objects the size of P/2019 LD$_2$ in the transition region at any given time.

Based on observations with the NASA/ESA Hubble Space Telescope obtained from the Data Archive at the Space Telescope Science Institute, which is operated by the Association of Universities for Research in Astronomy, Incorporated, under NASA contracts NAS5-26555. Support for Program number (GO 16077) was provided through a grant from the STScI under NASA contract NAS5-26555.

This work is based on observations made with the Spitzer Space Telescope, which was operated by the Jet Propulsion Laboratory, California Institute of Technology, under a contract with NASA.

Based on observations obtained with the Samuel Oschin Telescope 48-inch and the 60-inch Telescope at the Palomar Observatory as part of the Zwicky Transient Facility project. ZTF is supported by the National Science Foundation under Grant No. AST-1440341 and a collaboration including Caltech, IPAC, the Weizmann Institute for Science, the Oskar Klein Center at Stockholm University, the University of Maryland, the University of Washington, Deutsches Elektronen-Synchrotron and Humboldt University, Los Alamos National Laboratories, the TANGO Consortium of Taiwan, the University of Wisconsin at Milwaukee, and Lawrence Berkeley National Laboratories. Operations are conducted by COO, IPAC, and UW.

The Liverpool Telescope is operated on the island of La Palma by Liverpool John Moores University in the Spanish Observatorio del Roque de los Muchachos of the Instituto de Astrofisica de Canarias with financial support from the UK Science and Technology Facilities Council.

This work was supported by the GROWTH project funded by the National Science Foundation under PIRE Grant No 1545949.

Some of the data presented herein were obtained at the W. M. Keck Observatory, which is operated as a scientific partnership among the California Institute of Technology, the University of California and the National Aeronautics and Space Administration. The Observatory was made possible by the generous financial support of the W. M. Keck Foundation.

The authors wish to recognize and acknowledge the very significant cultural role and reverence that the summit of Maunakea has always had within the indigenous Hawaiian community. We are most fortunate to have the opportunity to conduct observations from this mountain.

B.T.B., G.H. and F.J.M. acknowledge support from NASA with grant number 80NSSC19K0780.

C.F. gratefully acknowledges the support of his research by the Heising-Simons Foundation (#2018-0907).

M. W. Coughlin acknowledges support from the National Science Foundation with grant number PHY-2010970.

This publication has made use of data collected at Lulin Observatory, partly supported by MoST grant 108-2112-M-008-001.

C.C.N. thanks to the funding from MOST grant 104-2923-M-008-004-MY5.

The authors would like to acknowledge the helpful discussion of P/2019 LD$_2$ with L. Woodney and Q.-Z. Ye.

This work has made use of data from the European Space Agency (ESA) mission *Gaia* (`https://www.cosmos.esa.int/gaia`), processed by the *Gaia* Data Processing and Analysis Consortium (DPAC, `https://www.cosmos.esa.int/web/gaia/dpac/consortium`). Funding for the DPAC has been provided by national institutions, in particular the institutions participating in the *Gaia* Multilateral Agreement.

Facility: *Hubble Space Telescope*, *Spitzer Space Telescope*, Keck I Telescope, P48 Oschin Schmidt telescope/Zwicky Transient Facility, Apache Point Astrophysical Research Consortium 3.5 m telescope, Liverpool Telescope, Lulin Optical Telescope, Mount Laguna Observatory 40-inch Telescope

Software: Small Body Python, ZChecker, LPipe

REFERENCES

A'Hearn, M. F. 1982, in IAU Colloq. 61: Comet Discoveries, Statistics, and Observational Selection, ed. L. L. Wilkening, 433–460

A'Hearn, M. F., Millis, R. C., Schleicher, D. O., Osip, D. J., & Birch, P. V. 1995, Icarus, 118, 223, doi: 10.1006/icar.1995.1190

A'Hearn, M. F., Schleicher, D. G., Millis, R. L., Feldman, P. D., & Thompson, D. T. 1984, AJ, 89, 579, doi: 10.1086/113552

Bauer, J. M., Grav, T., Blauvelt, E., et al. 2013, ApJ, 773, 22, doi: 10.1088/0004-637X/773/1/22

Bauer, J. M., Stevenson, R., Kramer, E., et al. 2015, ApJ, 814, 85, doi: 10.1088/0004-637X/814/2/85

Bellm, E. C., Kulkarni, S. R., Graham, M. J., et al. 2019, 131, 018002, doi: 10.1088/1538-3873/aaecbe

Boe, B., Jedicke, R., Meech, K. J., et al. 2019, Icarus, 333, 252, doi: 10.1016/j.icarus.2019.05.034

Bohren, C. F., & Huffman, D. R. 1983, Absorption and scattering of light by small particles

Bolin, B., Fernandez, Y., Bauer, J., Helou, G., & Lisse, C. 2019a, Spitzer investigation of the first known active Trojan, 2019 LD2, Spitzer Proposal

Bolin, B. T., Bodewits, D., Fernandez, Y., & Lisse, C. M. 2019b, Constraining the coma volatile content of interstellar comet 2I/Borisov, HST Proposal

Bolin, B. T., & Lisse, C. M. 2020, MNRAS, 497, 4031, doi: 10.1093/mnras/staa2192

Bolin, B. T., Weaver, H. A., Fernandez, Y. R., et al. 2018, ApJL, 852, L2, doi: 10.3847/2041-8213/aaa0c9

Bolin, B. T., Lisse, C. M., Kasliwal, M. M., et al. 2020a, AJ, 160, 26, doi: 10.3847/1538-3881/ab9305

—. 2020b, AJ, 160, 26, doi: 10.3847/1538-3881/ab9305

Bolin, B. T., Fremling, C., Holt, T. R., et al. 2020, ApJL, 900, L45

Brasser, R., & Wang, J. H. 2015, A&A, 573, A102, doi: 10.1051/0004-6361/201423687

Burns, J. A., Lamy, P. L., & Soter, S. 1979, Icarus, 40, 1, doi: 10.1016/0019-1035(79)90050-2

Combi, M. R., Harris, W. M., & Smyth, W. H. 2004, Gas dynamics and kinetics in the cometary coma: theory and observations, ed. M. C. Festou, H. U. Keller, & H. A. Weaver, 523

De Sanctis, M. C., Capria, M. T., Coradini, A., & Orosei, R. 2000, AJ, 120, 1571, doi: 10.1086/301512

DeMeo, F. E., & Carry, B. 2013, Icarus, 226, 723, doi: 10.1016/j.icarus.2013.06.027

Deustua, S. E., Mack, J., Bajaj, V., & Khandrika, H. 2017, WFC3/UVIS Updated 2017 Chip-Dependent Inverse Sensitivity Values, Tech. rep.

Dones, L., Brasser, R., Kaib, N., & Rickman, H. 2015, SSRv, 197, 191, doi: 10.1007/s11214-015-0223-2

Dressel, L. 2012, Wide Field Camera 3 Instrument Handbook for Cycle 21 v. 5.0

Duncan, M., Levison, H., & Dones, L. 2004, Dynamical evolution of ecliptic comets, ed. M. C. Festou, H. U. Keller, & H. A. Weaver, 193

Farnham, T. L., Schleicher, D. G., & A'Hearn, M. F. 2000, Icarus, 147, 180, doi: 10.1006/icar.2000.6420

Fazio, G. G., Hora, J. L., Allen, L. E., et al. 2004, ApJS, 154, 10, doi: 10.1086/422843

Feldman, P. D., Cochran, A. L., & Combi, M. R. 2004, Spectroscopic investigations of fragment species in the coma, ed. M. C. Festou, H. U. Keller, & H. A. Weaver, 425

Fernández, Y. R. 2009, Planet. Space Sci., 57, 1218, doi: 10.1016/j.pss.2009.01.003

Fernández, Y. R., Kelley, M. S., Lamy, P. L., et al. 2013, Icarus, 226, 1138, doi: 10.1016/j.icarus.2013.07.021

Fitzsimmons, A., Young, D., Armstrong, J., Moss, S., & Sato, H. 2020, Minor Planet Electronic Circulars, 2020-K134, 1

Gladman, B., Marsden, B. G., & Vanlaerhoven, C. 2008, Nomenclature in the Outer Solar System, ed. M. A. Barucci, H. Boehnhardt, D. P. Cruikshank, A. Morbidelli, & R. Dotson, 43–57

Graham, M. J., Kulkarni, S. R., Bellm, E. C., et al. 2019, PASP, 131, 078001, doi: 10.1088/1538-3873/ab006c

Gunnarsson, M., Bockelée-Morvan, D., Biver, N., Crovisier, J., & Rickman, H. 2008, A&A, 484, 537, doi: 10.1051/0004-6361:20078069

Hanuš, J., Delbo, M., Alí-Lagoa, V., et al. 2018, Icarus, 299, 84, doi: 10.1016/j.icarus.2017.07.007

Haser, L. 1957, Bulletin de la Societe Royale des Sciences de Liege, 43, 740

Holt, T. R., Nesvorný, D., Horner, J., et al. 2020, Mon. Not. R. Astron. Soc., 495, 4085, doi: 10.1093/mnras/staa1348

Horner, J., & Evans, N. W. 2006, MNRAS, 367, L20, doi: 10.1111/j.1745-3933.2006.00131.x

Horner, J., Evans, N. W., & Bailey, M. E. 2004, Mon. Not. R. Astron. Soc., 354, 798, doi: 10.1111/j.1365-2966.2004.08240.x

Horner, J., Evans, N. W., & Bailey, M. E. 2004, MNRAS, 355, 321, doi: 10.1111/j.1365-2966.2004.08342.x

Horner, J., & Lykawka, P. S. 2012, MNRAS, 426, 159, doi: 10.1111/j.1365-2966.2012.21717.x

Hsieh, H. H., Fitzsimmons, A., Novaković, B., Denneau, L., & Heinze, A. N. 2021, Icarus, 354, 114019, doi: 10.1016/j.icarus.2020.114019

Hsieh, H. H., Denneau, L., Wainscoat, R. J., et al. 2015a, Icarus, 248, 289, doi: 10.1016/j.icarus.2014.10.031

Hsieh, H. H., Hainaut, O., Novaković, B., et al. 2015b, ApJL, 800, L16, doi: 10.1088/2041-8205/800/1/L16

Huehnerhoff, J., Ketzeback, W., Bradley, A., et al. 2016, in Proc. SPIE, Vol. 9908, Ground-based and Airborne Instrumentation for Astronomy VI, 99085H

Ivanova, O., Borysenko, S., & Golovin, A. 2014, Icarus, 227, 202, doi: 10.1016/j.icarus.2013.08.026

Ivanova, O. V., Skorov, Y. V., Korsun, P. P., Afanasiev, V. L., & Blum, J. 2011, Icarus, 211, 559, doi: 10.1016/j.icarus.2010.10.026

Ivezić, Ž., Tabachnik, S., Rafikov, R., et al. 2001, AJ, 122, 2749, doi: 10.1086/323452

Ivezić, Ž., Lupton, R. H., Jurić, M., et al. 2002, AJ, 124, 2943, doi: 10.1086/344077

Jedicke, R., Bolin, B., Granvik, M., & Beshore, E. 2016, Icarus, 266, 173, doi: 10.1016/j.icarus.2015.10.021

Jewitt, D. 2015, AJ, 150, 201, doi: 10.1088/0004-6256/150/6/201

Jewitt, D., Hsieh, H., & Agarwal, J. 2015, The Active Asteroids, ed. P. Michel, F. E. DeMeo, & W. F. Bottke, 221–241

Jewitt, D., Ishiguro, M., Weaver, H., et al. 2014, AJ, 147, 117, doi: 10.1088/0004-6256/147/5/117

Jewitt, D. C. 2009, in European Planetary Science Congress 2009, 13

Jewitt, D. C., & Meech, K. J. 1987, ApJ, 317, 992, doi: 10.1086/165347

Jordi, K., Grebel, E. K., & Ammon, K. 2006, A&A, 460, 339, doi: 10.1051/0004-6361:20066082

Jurić, M., Ivezić, Ž., Lupton, R. H., et al. 2002, AJ, 124, 1776, doi: 10.1086/341950

Kareta, T., Sharkey, B., Noonan, J., et al. 2019, AJ, 158, 255, doi: 10.3847/1538-3881/ab505f

Kasliwal, M. M., Cannella, C., Bagdasaryan, A., et al. 2019, PASP, 131, 038003, doi: 10.1088/1538-3873/aafbc2

Kelley, M. S., Fernández, Y. R., Licandro, J., et al. 2013, Icarus, 225, 475, doi: 10.1016/j.icarus.2013.04.012

Kelley, M. S. P., Bodewits, D., Ye, Q., et al. 2019, in Astronomical Society of the Pacific Conference Series, Vol. 523, Astronomical Data Analysis Software and Systems XXVII, ed. P. J. Teuben, M. W. Pound, B. A. Thomas, & E. M. Warner, 471

Kinoshita, D., Chen, C.-W., Lin, H.-C., et al. 2005, ChJA&A, 5, 315, doi: 10.1088/1009-9271/5/3/011

Krist, J. E., Hook, R. N., & Stoehr, F. 2011, in Society of Photo-Optical Instrumentation Engineers (SPIE) Conference Series, Vol. 8127, Optical Modeling and Performance Predictions V, 81270J

Levison, H. F., & Duncan, M. J. 1994, Icarus, 108, 18, doi: 10.1006/icar.1994.1039

Licandro, J., Pinilla-Alonso, N., de Leon, J., et al. 2020, in AAS/Division for Planetary Sciences Meeting Abstracts, Vol. 52, AAS/Division for Planetary Sciences Meeting Abstracts, 404.06

Lin, Z.-Y., Cheng, Y.-L., Vincent, J.-B., et al. 2020, PASJ, doi: 10.1093/pasj/psaa069

Lisse, C., Bauer, J., Cruikshank, D., et al. 2020, Nature Astronomy, 4, 930, doi: 10.1038/s41550-020-01219-6

Lisse, C. M., Young, L. A., Cruikshank, D., Sandford, S., & Schmitt, B. 2019, Submitted to Icarus

Lisse, C. M., Young, L. A., Cruikshank, D. P., et al. 2020, arXiv e-prints, arXiv:2009.02277. https://arxiv.org/abs/2009.02277

Marzari, F., Scholl, H., Murray, C., & Lagerkvist, C. 2002, Origin and Evolution of Trojan Asteroids, 725–738

Masci, F. J., Laher, R. R., Rusholme, B., et al. 2019, PASP, 131, 018003, doi: 10.1088/1538-3873/aae8ac

McCarthy, J. K., Cohen, J. G., Butcher, B., et al. 1998, Society of Photo-Optical Instrumentation Engineers (SPIE) Conference Series, Vol. 3355, Blue channel of the Keck low-resolution imaging spectrometer, ed. S. D'Odorico, 81–92

McDonnell, J. A. M., Alexander, W. M., Burton, W. M., et al. 1986, Nature, 321, 338, doi: 10.1038/321338a0

Meech, K. J., & Svoren, J. 2004, Using cometary activity to trace the physical and chemical evolution of cometary nuclei, ed. M. C. Festou, H. U. Keller, & H. A. Weaver, 317

Mommert, M., Kelley, M., de Val-Borro, M., et al. 2019, The Journal of Open Source Software, 4, 1426, doi: 10.21105/joss.01426

Morbidelli, A., Levison, H. F., Tsiganis, K., & Gomes, R. 2005, Nature, 435, 462, doi: 10.1038/nature03540

Moreno, F., Pozuelos, F. J., Novaković, B., et al. 2017, ApJL, 837, L3, doi: 10.3847/2041-8213/aa6036

Murray, C. D., & Dermott, S. F. 1999, Solar system dynamics

Nesvorný, D., Parker, J., & Vokrouhlický, D. 2018, AJ, 155, 246, doi: 10.3847/1538-3881/aac01f

Nesvorný, D., Vokrouhlický, D., Dones, L., et al. 2017, ApJ, 845, 27, doi: 10.3847/1538-4357/aa7cf6

Ofek, E. O. 2012, The Astrophysical Journal, 749, 10

Oke, J. B., Cohen, J. G., Carr, M., et al. 1995, PASP, 107, 375, doi: 10.1086/133562

O'Rourke, L., Heinisch, P., Blum, J., et al. 2020, Nature, 586, 697, doi: 10.1038/s41586-020-2834-3

Perley, D. A. 2019, PASP, 131, 084503, doi: 10.1088/1538-3873/ab215d

Reach, W. T., Kelley, M. S., & Vaubaillon, J. 2013, Icarus, 226, 777, doi: 10.1016/j.icarus.2013.06.011

Rein, H., & Liu, S.-F. 2012, Astron. Astrophys., 537, A128, doi: 10.1051/0004-6361/201118085

Rein, H., Hernandez, D. M., Tamayo, D., et al. 2019, Mon. Not. R. Astron. Soc., 485, 5490, doi: 10.1093/mnras/stz769

Roig, F., & Nesvorný, D. 2015, AJ, 150, 186, doi: 10.1088/0004-6256/150/6/186

Sarid, G., & Prialnik, D. 2009, Meteoritics and Planetary Science, 44, 1905, doi: 10.1111/j.1945-5100.2009.tb02000.x

Sarid, G., Volk, K., Steckloff, J. K., et al. 2019, ApJL, 883, L25, doi: 10.3847/2041-8213/ab3fb3

Sato, H., Heinze, A., & Nakano, S. 2020, Central Bureau Electronic Telegrams, 4780, 1

Schambeau, C., Fernandez, Y., Belton, R., et al. 2020, Central Bureau Electronic Telegrams, 4821, 1

Schambeau, C. A., Fernández, Y. R., Samarasinha, N. H., Woodney, L. M., & Kundu, A. 2019, AJ, 158, 259, doi: 10.3847/1538-3881/ab53e2

Schleicher, D. G., & Bair, A. N. 2011, AJ, 141, 177, doi: 10.1088/0004-6256/141/6/177

Smith, C. E., & Nelson, B. 1969, PASP, 81, 74, doi: 10.1086/128742

Solontoi, M., Ivezić, Ž., Jurić, M., et al. 2012, Icarus, 218, 571, doi: 10.1016/j.icarus.2011.10.008

Steckloff, J., Sarid, G., Volk, K., et al. 2020, arXiv e-prints, arXiv:2008.02943. https://arxiv.org/abs/2008.02943

Steckloff, J., Sarid, G., Volk, K., et al. 2020, 2. https://arxiv.org/abs/2008.02943

Steele, I. A., Smith, R. J., Rees, P. C. T., et al. 2004, in SPIE Astronomical Telescopes + Instrumentation

Tonry, J. L. 2011, PASP, 123, 58, doi: 10.1086/657997

Vokrouhlický, D., Nesvorný, D., & Dones, L. 2019, AJ, 157, 181, doi: 10.3847/1538-3881/ab13aa

Vokrouhlický, D., Pravec, P., Durech, J., et al. 2017, A&A, 598, A91, doi: 10.1051/0004-6361/201629670

Werner, M. W., Roellig, T. L., Low, F. J., et al. 2004, ApJS, 154, 1, doi: 10.1086/422992

Woodney, L., Kareta, T., Schambeau, C., et al. 2020, in AAS/Division for Planetary Sciences Meeting Abstracts, Vol. 52, AAS/Division for Planetary Sciences Meeting Abstracts, 404.05

Ye, Q., Kelley, M. S. P., Bodewits, D., et al. 2019, The Astronomer's Telegram, 12450

Table 1. Summary of P/2019 LD$_2$ target observations viewing geometry.

Date^1 UTC	Facility^2	Filter^3	θ_s^4 ($''$)	χ_{am}^5	r_H^6 (au)	Δ^7 (au)	α^8 (°)	δ_E^9 (°)	$T - T_p^{10}$ (days)
2019 Apr 26	ZTF[I]	r	2.17	1.76	4.693	4.147	10.99	-1.56	-343.97
2019 Sep 07	ARC	g,r	1.4	1.81	4.622	4.279	12.23	-0.74	-216.58
2020 Jan 25-26	*Spitzer*	4.5 μm	–	–	4.584	4.256[II]	12.61[II]	0.23[II]	-76.58
2020 Apr 01	*HST*	F350LP	–	–	4.578	5.023	10.71	-0.44	-9.58
2020 May 27	MLO 1.0-m	B,V,R	1.92	1.49	4.580	4.221	12.38	-2.50	46.42
2020 May 29	LT	g,r,i,z	1.21	1.75	4.580	4.193	12.27	-2.56	48.42
2020 June 23-27	LOT	B,V,R	1.47	1.14	4.583	3.848	9.59	-3.00	75.42
2020 July 10	LOT	B,V,R	1.45	1.15	4.586	3.707	7.11	-2.97	90.42
2020 Aug 19	Keck I	Sp.[III]	0.85	1.80	4.594	3.608	3.20	-1.76	130.42

Table 1. Columns: (1) observation date; (2) observational facility; (3) filter (for the Keck I observations, the B600/4000 grism and R600/7500 grating are used with the LRIS instrument[II] ; (4) in-image seeing of observations; (5) airmass of observations; (6) heliocentric distance; (7) topo-centric distance; (8) phase angle; (9) topo-centric and target orbital plane angle; (10) difference between time of observation T and time of perihelion T_p

Table 2. Summary of ZTF P/2019 LD$_2$ photometry.

Date^1 UTC	r_H^2 (au)	Δ^3 (au)	α^4 (°)	$T - T_p^5$ (days)	filter^6	mag^7	σ_{mag}^8	θ_s^9 ($''$)	χ_{am}^{10}	A(0°)$f\rho^{11}$ (cm)	C^{12} (km^2)
2019 Apr 09 - 10:32	4.704	4.391	12.0	-360.20	r	19.33	0.15	2.36	1.72	85.28	127.69
2019 Apr 12 - 10:32	4.702	4.345	11.9	-357.32	r	19.27	0.16	2.83	1.66	87.90	131.53
2019 Apr 15 - 09:59	4.700	4.300	11.7	-354.47	r	19.13	0.15	1.82	2.02	97.23	145.35
2019 Apr 20 - 09:33	4.697	4.227	11.4	-349.70	r	18.97	0.23	1.87	1.83	107.69	160.77
2019 Apr 20 - 10:04	4.697	4.226	11.4	-349.68	r	18.83	0.23	2.44	1.51	122.45	182.81
2019 Apr 26 - 09:00	4.693	4.142	11.0	-343.97	g	19.69	0.14	2.14	1.91	83.20	124.00
2019 Apr 26 - 09:07	4.693	4.142	11.0	-343.96	g	19.38	0.13	2.18	2.12	110.69	164.97
2019 Apr 26 - 11:26	4.693	4.141	11.0	-343.87	r	18.89	0.07	1.90	1.41	109.63	163.38
2019 Apr 26 - 11:36	4.693	4.141	11.0	-343.86	r	19.18	0.07	1.68	1.37	83.93	125.08
2019 May 02 - 10:03	4.689	4.061	10.4	-338.17	r	18.95	0.11	2.47	1.56	97.64	145.18
2019 May 02 - 10:32	4.689	4.061	10.4	-338.15	r	18.99	0.09	1.82	1.41	94.11	139.93

Continued on next page

[I] Serendipitous observation of P/2019 LD$_2$ with ZTF, but included in this table because of its inclusion in the top-left panel of Fig. 1.

[II] *Spitzer*-centric

[III] `https://www2.keck.hawaii.edu/inst/lris/filters.html`

Table 2 – *Continued from previous page*

Date[1] UTC	r_H[2] (au)	Δ[3] (au)	α[4] (°)	$T - T_p$[5] (days)	filter[6]	mag[7]	σ_{mag}[8]	θ_s[9] ($''$)	χ_{am}[10]	A(0°)$f\rho$[11] (cm)	C[12] (km^2)
2019 May 31 - 08:22	4.672	3.763	6.1	-310.33	r	18.76	0.07	1.60	1.44	85.34	125.82
2019 May 31 - 10:34	4.672	3.762	6.1	-310.24	g	18.96	0.07	1.79	1.44	112.44	165.78
2019 Jun 01 - 09:04	4.671	3.755	6.0	-309.33	r	18.57	0.05	1.78	1.38	100.81	148.64
2019 Jun 02 - 09:34	4.671	3.748	5.8	-308.35	r	18.49	0.07	2.53	1.37	107.32	158.24
2019 Jun 02 - 10:57	4.671	3.748	5.8	-308.29	g	18.95	0.08	1.93	1.52	111.35	164.18
2019 Jun 03 - 11:33	4.670	3.741	5.6	-307.30	g	18.52	0.18	1.99	1.71	163.56	241.16
2019 Jun 04 - 07:01	4.670	3.736	5.5	-306.52	r	18.06	0.06	2.07	1.67	156.64	230.96
2019 Jun 04 - 08:31	4.670	3.736	5.5	-306.46	g	18.68	0.09	2.55	1.40	140.25	206.79
2019 Jun 06 - 06:37	4.668	3.725	5.1	-304.60	r	18.36	0.08	1.99	1.77	116.28	171.48
2019 Jun 06 - 08:33	4.668	3.724	5.1	-304.53	g	18.63	0.09	2.11	1.39	143.63	211.82
2019 Jun 07 - 09:33	4.668	3.719	4.9	-303.52	r	18.14	0.06	1.87	1.39	140.87	207.78
2019 Jun 08 - 06:36	4.667	3.714	4.8	-302.67	r	18.57	0.09	1.90	1.73	94.15	138.88
2019 Jun 08 - 09:12	4.667	3.713	4.8	-302.57	g	18.56	0.08	2.07	1.37	150.52	222.03
2019 Jun 09 - 06:36	4.667	3.709	4.6	-301.71	r	18.38	0.06	1.89	1.70	111.02	163.79
2019 Jun 10 - 07:02	4.666	3.704	4.5	-300.72	r	18.34	0.06	1.90	1.56	114.39	168.78
2019 Jun 10 - 08:03	4.666	3.704	4.5	-300.68	g	18.70	0.10	2.27	1.40	130.13	192.01
2019 Jun 11 - 09:43	4.666	3.699	4.3	-299.65	g	18.90	0.10	1.93	1.42	107.13	158.11
2019 Jun 14 - 08:02	4.664	3.688	3.9	-296.81	g	18.74	0.22	2.03	1.38	121.43	179.30
2019 Jun 20 - 07:50	4.661	3.673	3.3	-291.02	g	18.61	0.22	2.51	1.38	132.47	195.84
2019 Jun 20 - 08:17	4.661	3.673	3.3	-291.00	r	18.15	0.10	1.97	1.37	127.68	188.75
2019 Jun 23 - 09:02	4.659	3.669	3.2	-288.07	r	18.23	0.08	2.41	1.43	117.79	174.17
2019 Jun 23 - 10:34	4.659	3.669	3.2	-288.00	g	18.77	0.18	2.57	1.84	113.53	167.87
2019 Jun 26 - 07:37	4.657	3.667	3.2	-285.22	r	18.21	0.05	1.87	1.37	119.75	177.06
2019 Jun 26 - 08:02	4.657	3.667	3.2	-285.20	g	18.80	0.08	2.19	1.38	110.22	162.98
2019 Jul 01 - 06:45	4.655	3.671	3.5	-280.41	r	18.33	0.05	1.84	1.40	108.62	160.51
2019 Jul 01 - 06:46	4.655	3.671	3.5	-280.41	r	18.33	0.05	1.77	1.39	108.62	160.51
2019 Jul 01 - 07:44	4.655	3.671	3.5	-280.37	r	18.34	0.06	2.37	1.38	107.63	159.04
2019 Jul 01 - 07:44	4.655	3.671	3.5	-280.37	r	18.34	0.06	2.18	1.38	107.63	159.04
2019 Jul 03 - 07:10	4.654	3.674	3.8	-278.45	r	18.17	0.05	2.31	1.37	127.49	188.29
2019 Jul 03 - 07:32	4.654	3.674	3.8	-278.44	g	18.58	0.07	2.14	1.37	138.51	204.56
2019 Jul 04 - 07:36	4.653	3.676	3.9	-277.46	r	18.09	0.05	2.04	1.38	137.86	203.57
2019 Jul 06 - 06:43	4.652	3.681	4.2	-275.56	g	18.74	0.09	1.92	1.38	121.73	179.68
2019 Jul 08 - 07:32	4.651	3.687	4.5	-273.59	g	18.48	0.07	1.92	1.39	156.89	231.49
2019 Jul 09 - 05:29	4.651	3.690	4.6	-272.70	r	18.13	0.04	1.58	1.48	137.39	202.69
2019 Jul 09 - 07:36	4.651	3.690	4.6	-272.61	g	18.61	0.07	1.84	1.40	139.94	206.46
2019 Jul 10 - 06:01	4.650	3.694	4.8	-271.71	r	18.21	0.06	2.02	1.41	128.82	190.02
2019 Jul 10 - 06:02	4.650	3.694	4.8	-271.71	r	18.06	0.06	2.30	1.41	147.90	218.17
2019 Jul 10 - 06:13	4.650	3.694	4.8	-271.70	r	18.27	0.06	1.96	1.39	121.89	179.80

Continued on next page

Table 2 – *Continued from previous page*

Date[1] UTC	r_H[2] (au)	Δ[3] (au)	α[4] (°)	$T - T_p$[5] (days)	filter[6]	mag[7]	$\sigma_{\rm mag}$[8]	θ_s[9] ($''$)	χ_{am}[10]	A(0°)$f\rho$[11] (cm)	C[12] (km^2)
2019 Jul 10 - 06:31	4.650	3.694	4.8	-271.69	*r*	18.20	0.07	2.44	1.38	130.01	191.77
2019 Jul 10 - 06:41	4.650	3.694	4.8	-271.68	*r*	18.15	0.05	2.04	1.37	136.14	200.81
2019 Jul 10 - 06:42	4.650	3.694	4.8	-271.68	*r*	18.18	0.06	2.14	1.37	132.43	195.34
2019 Jul 11 - 07:29	4.649	3.698	4.9	-270.68	*g*	18.70	0.13	1.90	1.40	130.73	192.82
2019 Jul 12 - 06:32	4.649	3.702	5.1	-269.74	*r*	18.23	0.11	2.46	1.37	128.40	189.36
2019 Jul 12 - 06:33	4.649	3.702	5.1	-269.74	*r*	18.25	0.10	2.35	1.37	126.06	185.90
2019 Jul 12 - 07:24	4.649	3.702	5.1	-269.71	*g*	18.53	0.15	2.01	1.40	154.37	227.66
2019 Jul 13 - 06:03	4.648	3.706	5.3	-268.79	*r*	18.12	0.10	2.49	1.39	143.40	211.46
2019 Jul 13 - 07:51	4.648	3.707	5.3	-268.72	*g*	18.80	0.24	1.69	1.45	121.56	179.25
2019 Jul 16 - 05:21	4.647	3.721	5.8	-265.91	*g*	18.57	0.28	2.10	1.39	154.15	227.28
2019 Jul 16 - 06:32	4.647	3.721	5.8	-265.86	*r*	18.26	0.16	1.92	1.39	129.40	190.79
2019 Jul 20 - 06:54	4.645	3.745	6.5	-261.96	*g*	18.65	0.16	2.67	1.45	148.69	219.26
2019 Jul 21 - 05:12	4.645	3.751	6.6	-261.05	*r*	18.22	0.04	1.52	1.38	140.36	206.99
2019 Jul 21 - 05:13	4.645	3.751	6.6	-261.05	*r*	18.18	0.04	1.58	1.38	145.63	214.76
2019 Jul 21 - 05:43	4.644	3.751	6.6	-261.03	*r*	18.17	0.05	1.44	1.37	146.91	216.66
2019 Jul 21 - 06:07	4.644	3.751	6.7	-261.01	*r*	18.34	0.05	1.46	1.38	126.07	185.94
2019 Jul 21 - 06:44	4.644	3.752	6.7	-260.99	*r*	18.35	0.09	2.67	1.43	124.98	184.33
2019 Jul 21 - 06:44	4.644	3.752	6.7	-260.99	*r*	18.31	0.08	2.71	1.44	129.68	191.25
2019 Jul 30 - 06:02	4.640	3.820	8.2	-252.26	*r*	18.21	0.05	1.85	1.42	155.19	229.33
2019 Jul 30 - 06:03	4.640	3.820	8.2	-252.26	*r*	18.20	0.04	1.70	1.42	156.63	231.45
2019 Jul 30 - 06:29	4.640	3.820	8.2	-252.24	*r*	18.27	0.05	1.92	1.49	146.85	217.00
2019 Jul 30 - 06:30	4.640	3.820	8.2	-252.24	*r*	18.30	0.05	1.82	1.49	142.85	211.08
2019 Aug 03 - 04:02	4.638	3.856	8.8	-248.45	*r*	18.31	0.10	1.65	1.40	147.13	217.68
2019 Aug 12 - 03:38	4.634	3.949	10.0	-239.69	*r*	18.11	0.16	3.23	1.39	192.88	286.40
2019 Aug 16 - 07:30	4.632	3.996	10.5	-235.63	*r*	18.34	0.16	1.83	1.78	162.34	241.48
2019 Aug 19 - 03:27	4.631	4.030	10.8	-232.87	*r*	18.33	0.09	1.41	1.38	168.23	250.52
2019 Aug 23 - 04:03	4.629	4.080	11.2	-228.94	*g*	18.73	0.09	1.80	1.39	191.39	285.49
2019 Aug 28 - 04:52	4.627	4.145	11.6	-224.02	*r*	18.34	0.06	1.73	1.54	180.68	269.98
2019 Aug 28 - 04:53	4.627	4.145	11.6	-224.02	*r*	18.37	0.06	1.78	1.54	175.75	262.63
2019 Aug 28 - 05:28	4.627	4.146	11.6	-223.99	*r*	18.43	0.06	1.56	1.71	166.38	248.63
2019 Aug 28 - 05:29	4.627	4.146	11.6	-223.99	*r*	18.51	0.06	1.68	1.72	154.56	230.97
2019 Aug 29 - 04:45	4.627	4.159	11.7	-223.05	*r*	18.37	0.06	2.22	1.53	177.51	265.38
2019 Aug 29 - 04:46	4.627	4.159	11.7	-223.05	*r*	18.43	0.07	2.42	1.53	167.97	251.11
2019 Aug 29 - 05:46	4.627	4.159	11.7	-223.00	*r*	18.37	0.06	1.60	1.86	177.51	265.38
2019 Aug 29 - 05:46	4.627	4.159	11.7	-223.00	*r*	18.38	0.06	1.62	1.87	175.88	262.95
2019 Aug 29 - 06:13	4.627	4.159	11.7	-222.99	*g*	18.85	0.14	1.96	2.13	180.81	270.31
2019 Sep 02 - 03:50	4.625	4.212	12.0	-219.17	*g*	18.94	0.11	1.84	1.43	172.19	257.81
2019 Sep 02 - 05:06	4.625	4.213	12.0	-219.12	*r*	18.56	0.09	2.20	1.70	154.25	230.94

Continued on next page

Table 2 – *Continued from previous page*

Date[1] UTC	r_H^2 (au)	Δ^3 (au)	α^4 (°)	$T - T_p^5$ (days)	filter[6]	mag[7]	$\sigma_{\rm mag}^8$	θ_s^9 (″)	χ_{am}^{10}	$A(0°)f\rho^{11}$ (cm)	C^{12} (km^2)
2019 Sep 03 - 03:40	4.624	4.226	12.0	-218.20	*g*	18.73	0.14	1.85	1.41	210.23	314.76
2019 Sep 09 - 03:04	4.622	4.309	12.3	-212.35	*g*	18.97	0.26	1.95	1.40	176.75	265.04
2019 Sep 09 - 05:38	4.622	4.311	12.3	-212.25	*r*	18.65	0.22	2.84	2.23	149.88	224.75
2019 Sep 25 - 03:09	4.616	4.540	12.5	-196.68	*r*	18.61	0.12	4.13	1.57	173.11	259.86
2019 Sep 25 - 04:55	4.616	4.542	12.5	-196.61	*g*	19.11	0.23	2.74	2.55	173.26	260.09
2019 Oct 01 - 03:35	4.614	4.628	12.4	-190.78	*g*	18.95	0.12	2.15	1.67	207.61	311.48
2019 Oct 09 - 02:21	4.611	4.742	12.2	-182.98	*g*	19.16	0.25	1.78	1.49	178.27	267.18
2019 Oct 12 - 02:42	4.610	4.785	12.0	-180.02	*r*	18.50	0.12	2.11	1.62	208.92	312.79
2019 Oct 16 - 02:42	4.608	4.840	11.8	-176.09	*g*	19.09	0.17	2.40	1.70	195.32	292.15
2019 Oct 19 - 02:09	4.607	4.881	11.6	-173.17	*r*	18.71	0.12	1.47	1.59	176.65	263.96
2019 Oct 19 - 02:36	4.607	4.882	11.6	-173.15	*g*	19.10	0.14	1.94	1.74	195.56	292.23
2019 Oct 22 - 02:40	4.606	4.922	11.4	-170.20	*g*	19.14	0.15	2.32	1.852	190.28	284.07
2019 Oct 26 - 02:30	4.605	4.975	11.1	-166.27	*g*	19.42	0.22	3.93	1.891	148.68	221.69
2019 Oct 26 - 02:35	4.605	4.975	11.1	-166.27	*r*	18.57	0.12	2.23	1.935	205.24	306.01
2019 Nov 08 - 01:48	4.601	5.135	9.9	-153.51	*r*	18.60	0.19	2.13	1.755	204.05	302.88

Table 2. Columns: (1) observation date; (2) heliocentric distance; (3) topo-centric distance; (4) phase angle; (5) difference between time of observation T and time of perihelion T_p; (6) filter; (7) 2×10^4 km aperture mag; (8) 1-σ mag uncertainty; (9) in-image seeing of observations; (10) airmass of observations; (11) $A(0°)f\rho$ of observations; (12) cross-section of observations